



Evaluation of an ϵ -manganese (IV) oxide/manganese vanadium oxide composite catalyst enriched with oxygen vacancies for enhanced formaldehyde removal

Xuan Liu^{a,b,1}, Jialin Wu^{a,1}, Shuai Zhang^c, Qiang Li^b, Zhaojun Wu^b, Jianbin Zhang^{a,b,*}

^a Hebei Provincial Key Lab of Green Chemical Technology and High Efficient Energy Saving, School of Chemical Engineering and Technology, Hebei University of Technology, Tianjin 300130, China

^b Inner Mongolia Engineering Research Center for CO₂ Capture and Utilization, Inner Mongolia University of Technology, Hohhot 010051, China

^c School of Materials Science and Engineering, Nankai University, Tianjin 300350, China

ARTICLE INFO

Keywords:

Formaldehyde
CO₂-storage material
 ϵ -MnO₂/Mn₂V₂O₇
Catalytic oxidation
Oxygen vacancies

ABSTRACT

Formaldehyde removal is vital to health, but the construction of high-performance non-precious metal catalysts still faces great challenges, in which increasing oxygen vacancies by dopant modification is an advanced strategy to enhance catalytic activity. In this work, a novel ϵ -MnO₂/Mn₂V₂O₇ composite catalyst with a synergistic effect was synthesized on the basis of a thermal decomposition strategy. Meanwhile, the precursor for the catalyst was synthesized from the reaction among CO₂-storage material, Mn²⁺, and vanadate without additional template agents and surfactants. Aided by the catalyst, the degradation rate of a 20 mg/L 10 mL formaldehyde (HCHO) solution can reach 72.0% and maintain above 67% after 5 cycles at 30 °C for 1 h. Subsequently, the as-obtained synergistic catalytic mechanism showed that the high-valent V⁵⁺ may partially replace Mn⁴⁺ in the MnO₂ framework, promoting the formation of enriched oxygen vacancies (V⁴⁺-□-Mn³⁺) on the surface of the composite catalyst via the redox coupling of Mn⁴⁺/Mn³⁺ and V⁵⁺/V⁴⁺. This leads to an increase in adsorbed oxygen, significantly improving the degradation performance of HCHO. This work provides a novel and advanced strategy for dopant modification to develop superior non-precious metal catalysts.

1. Introduction

As an important raw material, formaldehyde (HCHO) is often used in the pharmaceutical, paint, plastic, and textile industries [1,2]. However, with the rapid development of these industries, the HCHO concentration of some HCHO-containing wastewaters has reached tens of grams per liter. The discharge of this wastewater affects urban ecosystems and poses a great threat to human health; especially, HCHO has been identified as carcinogenic and teratogenic by the World Health Organization [3,4]. Therefore, the treatment of HCHO-containing wastewater has gradually become a popular research topic.

Most current research on HCHO removal from aqueous solutions has focused on 2 approaches: physical adsorption using porous materials at room temperature [5–7] and HCHO conversion to nontoxic and nonhazardous products (CO₂ and H₂O) using multiphase catalysts at

high temperatures [8,9]. Compared with physical adsorption, the catalytic oxidation of HCHO using multiphase catalysts is considered an emerging and promising method. Among them, the catalysts loaded with noble metals [10,11] can catalyze the oxidation of HCHO at lower temperatures; however, their high cost and little sources greatly limit the wide application of these loaded catalysts. Therefore, the development of low-cost and efficient catalysts for the removal of HCHO from aqueous solutions at room temperature remains a significant challenge. In recent years, some transition metal oxides, such as titanium dioxide (TiO₂) [12–15], cobalt oxide (Co₃O₄) [16], manganese oxides (MnO_x) [17], and binary oxides [18] were reported to be slightly more efficient for HCHO removal. Among these transition metal oxides, manganese dioxide (MnO₂) with a unit structure of [MnO₆] is considered as a promising catalyst owing to its abundant sources, environmental friendliness, and strong ability to remove HCHO [19]. Furthermore, the

* Corresponding author at: Hebei Provincial Key Lab of Green Chemical Technology and High Efficient Energy Saving, School of Chemical Engineering and Technology, Hebei University of Technology, Tianjin 300130, China.

E-mail address: tadzhang@pku.edu.cn (J. Zhang).

¹ These authors contributed equally to this work

<https://doi.org/10.1016/j.apcatb.2022.121994>

Received 12 August 2022; Received in revised form 6 September 2022; Accepted 15 September 2022

Available online 16 September 2022

0926-3373/© 2022 Elsevier B.V. All rights reserved.

different crystal structures of MnO_2 , such as α -, β -, γ -, λ -, δ - and ϵ - MnO_2 [20], can significantly affect its catalytic activity; however, most of the Mn-based catalysts are for the removal of HCHO gas, while the removal of HCHO from aqueous solutions at near room temperature is less reported. Therefore, it is necessary to optimize the structures of Mn-based catalysts for the improvement of the HCHO degradation capability from aqueous solutions. In the previous work of the group [21–23], the catalysts and adsorbents with excellent performance were optimized by single-factor and response surface experiments, which provide some references for the synthesis of efficient and stable Mn-based composite catalysts.

The outer electronic structure of Mn is $3d^5 4s^2$ and has multiple valence states ranging from -3 to $+7$ so that MnO_x can modulate electrons to generate the mobile electronic environment required for redox reactions [24]. Moreover, synergistic effects occur with doping of other transition metal oxides with MnO_x , leading to significantly enhanced oxygen vacancies with strong redox properties [25]. Recently, many transition metal cations may dop into the framework or tunneling of oxides, such as Cu^{2+} , Ni^{2+} , Co^{2+} , Fe^{3+} , Ti^{4+} , and Ce^{4+} , to increase their specific surface areas and oxygen vacancies. These doping changes their crystal structures and surface properties, resulting in highly active composite catalysts [26–29]. For example, Ma et al. [30] investigated Co-, Fe-, and Ce-doped cryptomelane-type MnO_x and found that the Ce-doped manganese oxide octahedral (Ce-OMS-2) structure with a large amount of Mn^{3+} , and oxygen vacancies had a high ozone removal efficiency at relatively high humidity. Du et al. [31] prepared a series of $\text{Mn}_x\text{Fe}_y/\text{Ac}$ composite catalysts using the static impregnation method and found that $\text{Mn}_{0.75}\text{Fe}_{0.02}/\text{Ac}$ exhibited better degradation of HCHO when the MnO_x and FeO_x synergies, and the interaction of Mn- FeO_x with the carrier was strong. However, the effect of doping with high-valent metal ions in the form of oxygen-containing anions on the crystal structure of MnO_2 may be more significant than that of doping with low-valent metal ions [32]. This is because the higher charge density of high-valent metal ions more easily activates the adsorbed oxygen molecules on the catalyst surface. Sui et al. [33] inserted high-valent vanadium ions (V^{5+}) into the framework of MnO_x , reducing the average oxidation state and forming more oxygen vacancies, thereby giving it great potential for catalysis. In addition, the V^{5+} ion radius is 0.54 \AA which is comparable with that in the $[\text{MnO}_6]$ framework (Mn^{3+} : 0.654 \AA and Mn^{4+} : 0.53 \AA); therefore, the probability of V^{5+} being doped into the MnO_2 structure is high [34]. To the best of our knowledge, V-doped MnO_2 has rarely been attempted for the catalytic oxidation of volatile organic compounds (VOCs) at room temperature, especially HCHO, and the structure of corresponding V-doped MnO_2 has rarely been discussed. Therefore, it is a great challenge to develop a V-doped MnO_2 composite catalyst enriched with oxygen vacancies and a well-defined structure for the degradation of HCHO from aqueous solutions at room temperature. In addition, the existing catalytic oxidation mechanism of gaseous HCHO, especially that of Mn-based materials, has been more abundant, which provides a corresponding reference for the catalytic oxidation mechanism of manganese-based catalytic materials in the aqueous solution. However, the mechanism in the removal of HCHO from aqueous solution by Mn-based materials is still unclear, and the corresponding explanation or description needs to be presented in conjunction with related studies.

In this study, $\text{MnCO}_3/\text{Mn}_2\text{V}_2\text{O}_7$ precursors were firstly synthesized using Mn^{3+} , VO_4^{3-} , and CO_2 -storage material (CO_2SM) in a simple one-step hydrothermal method without additional template agents and surfactants. CO_2SM was synthesized from CO_2 , 1,2-phenylenediamine (1,2-PPD), and 1,2-propanediamine (1,2-PDA) at room temperature. In this process, CO_2SM acted as a raw material and template agent during the hydrothermal process and provided the necessary environment for the formation of $\text{Mn}_2\text{V}_2\text{O}_7$. Subsequently, an ϵ - $\text{MnO}_2/\text{Mn}_2\text{V}_2\text{O}_7$ composite catalyst with enriched oxygen vacancies was fabricated by thermal decomposition, and the removal of HCHO at near room temperature was systematically investigated. The removal efficiency of ϵ - $\text{MnO}_2/$

$\text{Mn}_2\text{V}_2\text{O}_7$ composite catalyst reached 72.0% for a 20 mg/L 10 mL HCHO solution in 1 h, demonstrating a significant synergistic effect between ϵ - MnO_2 and $\text{Mn}_2\text{V}_2\text{O}_7$. Characterization of the catalyst demonstrated that V^{5+} ions were properly incorporated into the $[\text{MnO}_6]$ framework, thereby reducing the crystallinity of the sample, increasing the specific surface area, and enhancing the number of oxygen vacancies and adsorbed oxygen molecules on the surface; thus, the ability of the composite catalyst to degrade HCHO was improved. This study provides new strategies and ideas for doped Mn-based composite catalysts for the degradation of HCHO at room temperature.

2. Experimental

2.1. Preparation of ϵ - $\text{MnO}_2/\text{Mn}_2\text{V}_2\text{O}_7$

The $\text{MnCO}_3/\text{Mn}_2\text{V}_2\text{O}_7$ precursor was prepared by mixing 1.5 g CO_2SM (see Figs. S1 and S2) and Na_3VO_4 at a V–Mn molar ratio of 0.06 with 50 mL $c(\text{Mn}^{2+}) = 0.3 \text{ mol/L}$ solution in a 100 mL Teflon-lined stainless steel hydrothermal reactor that was sealed and heated at 120°C for 2 h. After the reactor cooled to room temperature, the precursor was washed with secondary water and ethanol thrice and dried at 120°C for 2 h. The solid was roasted at 320°C for 6 h in an air atmosphere to obtain the ϵ - $\text{MnO}_2/\text{Mn}_2\text{V}_2\text{O}_7$ composite catalyst. The reagent information is shown in [supporting information](#) (SI).

2.2. HCHO removal

The HCHO degradation performance of the composite catalyst was evaluated. Two 20 mg/L 10 mL HCHO solutions were placed in 2 different 50 mL round-bottom flasks in a constant-temperature water bath (IKA RCT Basic, $\pm 0.01^\circ\text{C}$) until the temperature stabilizes at 30°C . After temperature stabilization, 0.05 g of the catalyst was added to 1 flask, and the other was left without the catalyst and used as a blank control to estimate the error from the volatilization of the HCHO solution. After the catalytic reaction occurred for a certain period, both HCHO solutions were filtered with an aqueous filter membrane with a pore size of $0.22 \mu\text{m}$ and placed in a colorimetric tube. Subsequently, 2.5 mL of the reagent was added, and the mixture was shaken and heated in a water bath at $60 \pm 2^\circ\text{C}$ for 15 min. The absorbances were measured after cooling for 1 h, and the corresponding HCHO concentrations were calculated from the calibration curves (Fig. S3). The degradation rate of HCHO was calculated using the equation $\eta\% = (C_0 - C_t)/C_0$, where C_0 is the concentration of the HCHO solution in the blank control, and C_t is the concentration of HCHO solution at time, t.

3. Results and discussions

3.1. Preparation, formation mechanism and stability of composite catalysts

3.1.1. Influence of the preparation conditions of composite catalysts on HCHO removal

Influence of the V/Mn molar ratio: A series of $\text{MnCO}_3/\text{Mn}_2\text{V}_2\text{O}_7$ precursors were synthesized by varying V/Mn molar ratio (0.00, 0.03, 0.06, 0.09, 0.12, 0.15, 0.18, and 0.20) at $\text{CO}_2\text{SM} = 1.5 \text{ g}$, $c(\text{Mn}^{2+}) = 0.3 \text{ mol/L}$, $T = 120^\circ\text{C}$, and $t = 2 \text{ h}$. The precursors were roasted at 320°C for 6 h to obtain the corresponding catalysts C-V/ $\text{Mn}_{0.00}$, C-V/ $\text{Mn}_{0.03}$, C-V/ $\text{Mn}_{0.06}$, C-V/ $\text{Mn}_{0.09}$, C-V/ $\text{Mn}_{0.12}$, C-V/ $\text{Mn}_{0.15}$, C-V/ $\text{Mn}_{0.18}$, and C-V/ $\text{Mn}_{0.20}$.

Fig. 1(a) shows Fourier transform infrared (FTIR) spectra of ϵ - $\text{MnO}_2/\text{Mn}_2\text{V}_2\text{O}_7$ catalysts prepared with different V/Mn molar ratios. The intense characteristic peak at 580 cm^{-1} is caused by the symmetric stretching vibration of the Mn–O bond [35]. The broad peak at 3304 cm^{-1} is attributed to the symmetric stretching vibration of -OH in physisorbed water molecules, while the peak at 1647 cm^{-1} is viewed as the bending vibration of the adsorbed water molecules. The peak at

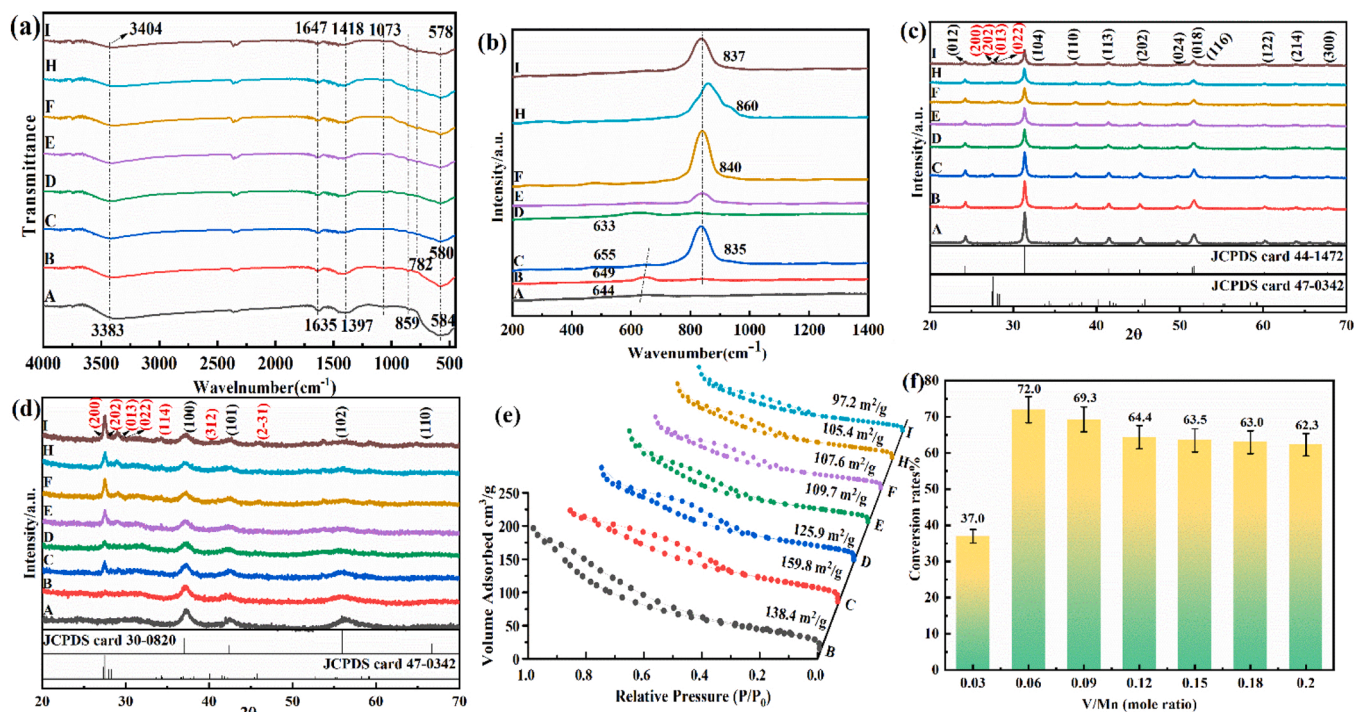


Fig. 1. (a) FTIR spectra, (b) Raman spectra, (c) XRD patterns of catalyst's precursors, (d) XRD patterns of catalysts, (e) N_2 adsorption-desorption isotherm, and (f) Degradation rate to 10 mL 20 mg/L HCHO solution at 30 °C. (A) C-V/ $Mn_{0.00}$, (B) C-V/ $Mn_{0.03}$, (C) C-V/ $Mn_{0.06}$, (D) C-V/ $Mn_{0.09}$, (E) C-V/ $Mn_{0.12}$, (F) C-V/ $Mn_{0.15}$, (H) C-V/ $Mn_{0.18}$ and (I) C-V/ $Mn_{0.20}$.

1073 cm^{-1} is associated with the stretching of the Mn^{3+} -O vibration [36] that indicates the presence of some Mn^{3+} in the structure of ϵ - MnO_2 / $Mn_2V_2O_7$. The characteristic peaks at 859 cm^{-1} and 782 cm^{-1} correspond to the symmetric stretching and bending vibrations of V-O-V [37,38], indicating that vanadium is properly integrated into the crystal phase of MnO_2 .

Fig. 1(b) shows Raman spectra of catalysts with multiple V/Mn molar ratios. The characteristic peaks between 630 and 655 cm^{-1} belong to the symmetric stretching vibrations of the Mn-O bond in the $[MnO_6]$ group of the ϵ - MnO_2 structural unit [39]. Additionally, when the V-doping amount is small, only the signal of the Mn-O bond is observed at the same frequency. When the V-doping amount increases, a strong characteristic peak that is due to the V-O vibration caused by the elongation of the V=O bond is observed at 840 cm^{-1} [34,40]. The Raman response of the V=O bond in pure V_2O_5 is generally at 1000 cm^{-1} [34,40], but there is no characteristic peak of the V=O bond between 970 and 1030 cm^{-1} , indicating that no additional vanadium framework compounds are formed in the catalyst [41,42]. In contrast, for the 3% V-doped sample, the vanadium content in the framework is low, and no V-O peaks are observed owing to the low Raman detection limit. As the V/Mn molar ratio increases, the characteristic peak at 630 cm^{-1} gradually weakens or disappears, indicating that the addition of vanadium led to the distortion of ϵ - MnO_2 crystal structure, and V^{5+} replaced Mn^{4+} in the $[MnO_6]$ structure [43]. Regarding samples with lower vanadium content, the characteristic peak at 630 cm^{-1} exhibits a certain shift, in which V-doping results in more oxygen vacancies [44]. The maximum Raman shift was observed at V/Mn = 0.06, indicating that the sample had the maximum Mn-O bond force constant (k), which can be calculated according to Hooke's law as $\omega = (k/\mu)^{1/2}/(2\pi c)$ [45], where ω represents the Raman shift (cm^{-1}), c is the speed of light, and μ is the effective mass. According to the literature [45], the catalytic performance of a single α - MnO_2 crystal is related to the bonding force constant of the Mn-O bond that affects the activity of lattice oxygen (O_{lat}) and plays an important role in the catalytic reaction. In addition, the high catalytic performance is also related to other factors, such as the

quantity of oxygen adsorbed onto the surface of the catalyst, the number of oxygen vacancies, and Mn^{3+} and V^{4+} contents.

Fig. 1(c) and (d) show X-ray diffraction (XRD) patterns for the precursors and catalysts prepared from multiple V/Mn molar ratios. All the diffraction peaks in Fig. 1(c) are indexed as calcite-type $MnCO_3$ (JCPDS No. 44-1427) and $Mn_2V_2O_7$ (JCPDS No. 47-0342) [46,47]. The special peaks located at 24.3°, 31.3°, 37.5°, 41.5°, 45.3°, 49.7°, 51.7°, 60.3°, 64.0°, and 67.8° belong to the (012), (014), (113), (202), (024), (018) (116), (122), (214), and (300) crystal planes of $MnCO_3$, respectively. Furthermore, the diffraction peaks at 27.4°, 27.5°, 28.0°, and 28.2° correspond to the (200), (022), (022), and (300) crystal planes of $Mn_2V_2O_7$, respectively. As shown in Fig. 1(c), the diffraction peaks of the $MnCO_3$ precursor are sharper, proving its regular lattice arrangement and good crystallinity. The diffraction peak of $Mn_2V_2O_7$ is not obvious due to the small amount of V-doping, but no other impurity peaks are observed, proving that the precursor is composed of $MnCO_3$ and $Mn_2V_2O_7$ crystals. With an increase in the V-doping amount, the diffraction peaks of the $MnCO_3$ precursors gradually become weaker and wider, indicating that the crystallinity of the precursors are reduced. After thermal decomposition, all the diffraction peaks in Fig. 1(d) are indexed as ϵ - MnO_2 (JCPDS No. 30-0820) [48] and $Mn_2V_2O_7$ (JCPDS No. 47-0342), where the diffraction peaks located at 37.1°, 42.3°, 56.4°, and 66.8° correspond to the (100), (011), (102), and (110) crystal planes of ϵ - MnO_2 , respectively. The positions of the $Mn_2V_2O_7$ diffraction peaks did not change, indicating that the nature of $Mn_2V_2O_7$ is stable during the roasting process. As shown in Fig. 1(d), the diffraction peaks of $Mn_2V_2O_7$ gradually increase with increasing V-doping amount, and the characteristic peaks of ϵ - MnO_2 still exist, but the intensity of the diffraction peaks become weaker or disappear. The characteristic peak at 37.1° is wider than that for the undoped sample, which proves that V-doping destroys the crystal structure of ϵ - MnO_2 , resulting in poor crystallinity, more structural defects, and stronger catalytic oxidation properties [49]. The grain sizes of different samples were calculated using Scherrer's equation to get 1.13 nm, 0.97 nm, 0.89 nm, 1.34 nm, 1.45 nm, 1.61 nm, and 1.67 nm, and the smallest catalyst grain size was

obtained at V/Mn = 0.06. The small grain size is beneficial in increasing the S_{BET} of the sample and exposing more oxygen vacancies [27,50–52].

Fig. 1(e) shows N_2 adsorption-desorption isotherms of the catalysts prepared at different V/Mn molar ratios, and the specific data are listed in Table 1. All catalysts exhibit type IV isotherms with H₄-type hysteresis loops in the relative pressure (P/P_0) of 0.7–1.0, indicating that the samples are mesoporous with slit-like homogeneous pores [53]. At V/Mn = 0.06, the composite catalyst possesses a specific surface area and pore volume of 159.8 m²/g and 0.2882 mL/g. Meanwhile, the S_{BET} of the sample increases and subsequently decreases with the increase of the V/Mn molar ratio. The increase in S_{BET} is attributed to V⁵⁺ ions replacing Mn⁴⁺ in [MnO₆] when the amount of vanadium used for doping is little, leading to deformation of the crystal structure, nucleus growth, and ϵ -MnO₂ interacting with Mn₂V₂O₇. When the V-doping amount is increased, it causes the samples to agglomerate and blocks the pore channels; thus, the S_{BET} decreases accordingly [54].

Fig. 1(f) shows degradation efficiency of the catalysts prepared at different V/Mn molar ratios for HCHO. The HCHO degradation efficiency of ϵ -MnO₂/Mn₂V₂O₇ increases and subsequently decreases with increasing V/Mn molar ratio, reaching a maximum value of 72% at V/Mn = 0.06. The trend of HCHO degradation efficiency corresponds well with the S_{BET} , indicating that a larger S_{BET} is favorable for HCHO to be adsorbed and degraded.

Fig. 2 shows XPS spectra of catalysts prepared with different V/Mn molar ratios (O 1 s, Mn 2p, and V 2p). The binding energies of Mn 2p_{1/2} and Mn 2p_{3/2} are found at 653.1 eV and 641.4 eV, with a spin-orbit splitting energy difference of 11.7 eV, which is closer to the theoretical value (11.8 eV), indicating that a +4 valence Mn exists in the catalyst [55]. The Mn 2p curves are fitted using the Avantage software, where the peaks at 641.4 and 653.1 eV are assigned to Mn³⁺, the peaks at 654.2 and 656.2 eV are assigned to Mn⁴⁺, and the Mn³⁺/Mn⁴⁺ ratio is calculated from the peak area and the data listed in Table 2. According to the literature [56], once Mn³⁺ appears in the catalyst, based on the principle of electroneutrality, corresponding oxygen vacancies generated to maintain the electrostatic equilibrium, $4Mn^{4+} + O^{2-} \rightarrow 4Mn^{4+} + 2e^-/\square + 0.5 O_2 \rightarrow 2Mn^{4+} + 2Mn^{3+} + \square + 0.5 O_2$, where \square represents the oxygen vacancies. Therefore, the higher Mn³⁺/Mn⁴⁺ ratio results in more oxygen vacancies in the catalyst that play a crucial role in the catalytic reaction. From Table 2, the Mn³⁺/Mn⁴⁺ ratio is largest at V/Mn = 0.06, representing the catalyst with the highest content of oxygen vacancies on its surface, which translates to the strongest catalytic activity. The average oxidation state (AOS) of Mn can be calculated based on the empirical equation [57]: $AOS = 8.956 - 1.126\Delta E$, where ΔE is the difference between the binding energies of the 2 characteristic peaks in the Mn 3s spectrum. The AOS value reaches a minimum at V/Mn = 0.06, indicating that the corresponding catalyst has the most abundant oxygen defects.

The O 1s spectrum is divided into 3 peaks at 295.5 eV, 531.5 eV, and 529.5 eV, using the Avantage software, corresponding to O_{latt}, surface adsorbed oxygen (O_{ads}), and adsorbed H₂O molecules [56]. According to Table 2, when V/Mn = 0.06, the ratio of O_{ads}/O_{latt} is largest, indicating that there is a large amount of adsorbed oxygen on the catalyst surface. According to the Mars–van Krevelen mechanism [58], the O_{latt} directly involved in the reaction can be rapidly regenerated by filling the O_{ads}.

Table 1

N_2 adsorption-desorption results of ϵ -MnO₂/Mn₂V₂O₇ prepared at different V/Mn molar ratios.

Catalysts (mole ratio)	$S_{BET}/m^2 \cdot g^{-1}$	Pore Volume/mL/g	Pore Size/nm
V/Mn = 0.03	138.4	0.259	8.33
V/Mn = 0.06	159.8	0.288	6.48
V/Mn = 0.09	125.9	0.238	7.55
V/Mn = 0.12	109.7	0.245	8.94
V/Mn = 0.15	107.6	0.211	8.01
V/Mn = 0.18	105.4	0.220	8.18
V/Mn = 0.20	97.2	0.207	8.53

Therefore, when V/Mn = 0.06, the abundant oxygen vacancies and O_{ads} species on the surface of the sample accelerate the mobility of O_{latt}, resulting in better catalytic performance. Based on the XPS spectrum of V 2p_{3/2}, the characteristic peaks at 518.5 eV and 516.8 eV belong to V⁵⁺ and V⁴⁺ [59–61]. As shown in Table 2, when V/Mn = 0.06, the ratio of V⁴⁺/V⁵⁺ is largest, indicating that the catalyst contains a large amount of V⁴⁺. Similarly, the presence of V⁴⁺ generates oxygen vacancies to maintain the electrostatic equilibrium $4V^{5+} + O^{2-} \rightarrow 4V^{5+} + 2e^-/\square + 0.5 O_2 \rightarrow 2V^{5+} + 2V^{4+} + \square + 0.5 O_2$ that facilitates the absorption of a large number of oxygen species and can be further converted to O_{latt}, promoting catalytic oxidation reactions.

The above results indicate that the catalytic performance of the composite catalyst ϵ -MnO₂/Mn₂V₂O₇ is affected by the doping amount of vanadium. The larger S_{BET} , strong Mn–O bond, and abundant oxygen vacancies lead to an optimum C-V/Mn_{0.06} HCHO degradation performance.

Effect of the hydrothermal temperature: A series of MnCO₃/Mn₂V₂O₇ precursors were synthesized by varying the hydrothermal temperature (80 °C, 100 °C, 120 °C, 140 °C, 160 °C, and 180 °C) at CO₂SM = 1.5 g, c (Mn²⁺) = 0.3 mol/L, V/Mn = 0.06 and t = 2 h. The precursors were roasted at 320 °C for 6 h to obtain the corresponding catalysts as C-T₈₀, C-T₁₀₀, C-T₁₂₀, C-T₁₄₀, C-T₁₆₀, and C-T₁₈₀.

Fig. S4(a) shows the FTIR spectra of catalysts formed at different hydrothermal temperatures. The characteristic peaks of ϵ -MnO₂/Mn₂V₂O₇ are obvious, showing that vanadium is well doped into the main crystal phase of ϵ -MnO₂. Meanwhile, a certain amount of adsorbed water and Mn³⁺ provides a basis for the degradation of HCHO. Fig. S4(b) shows the Raman spectra of a catalyst with a shift in the characteristic peak of the Mn–O bond from 645.7 cm^{−1} to 654.9 cm^{−1} at a hydrothermal temperature range of 80–120 °C, indicating that the interaction between ϵ -MnO₂ and Mn₂V₂O₇ is strengthened with the increasing temperature. Additionally, the distance between Mn and O atoms becomes shorter, making the O atoms in the ϵ -MnO₂ crystal move more easily [62]. When the temperature is increased, the characteristic peak of the Mn–O bond shifts from 649.4 cm^{−1} to 634.8 cm^{−1}, which may be because the crystal growth is denser at the higher temperature, weakening the interaction between Mn and O and the ability of the O atoms to move in the ϵ -MnO₂ crystal [62]. Therefore, the catalyst has an optimum catalytic performance at T = 120 °C.

From Fig. S4(c), an increase in hydrothermal temperature sharpens the diffraction peaks of the precursors and increases the crystallinity of the samples. As shown in Fig. S4(d), the characteristic peaks of Mn₂V₂O₇ are not obvious at the hydrothermal temperature range of 80–100 °C. The diffraction peaks of Mn₂V₂O₇ become sharp, and the crystallinity increases as the hydrothermal temperature increases to 120–180 °C, proving that the preparation conditions for the precursors significantly affect the structure of the composite catalysts [63].

According to Fig. S4(e), the as-prepared catalysts are mesoporous and show an increasing and subsequently decreasing trend in the investigated temperature range that can be attributed to the different nucleation rates of the crystals at different temperatures where the crystal growth is slow at lower temperatures, and the S_{BET} value increases with increasing temperature. As the temperature increases, the thermal motion of the solution accelerates, the crystal growth becomes denser, and the S_{BET} value decreases (Table S1). Furthermore, at T = 120 °C, the sample has the maximum S_{BET} . Fig. S4(f) shows that the degradation efficiency gradually increases between 80 and 120 °C and decreases between 140 and 180 °C, and the sample has an optimum degradation efficiency at T = 120 °C with a value of 72.0%, which corresponds to the S_{BET} value.

The chemical properties of the sample surfaces were characterized using XPS (Fig. S5 and Table S2). At T = 120 °C, the catalyst shows the highest O_{ads}/O_{latt}, Mn³⁺/Mn⁴⁺, and V⁴⁺/V⁵⁺ values, proving that the catalyst contains a large number of oxygen vacancies and various O_{ads} species.

Based on the results above, T = 120 °C was selected as the optimum

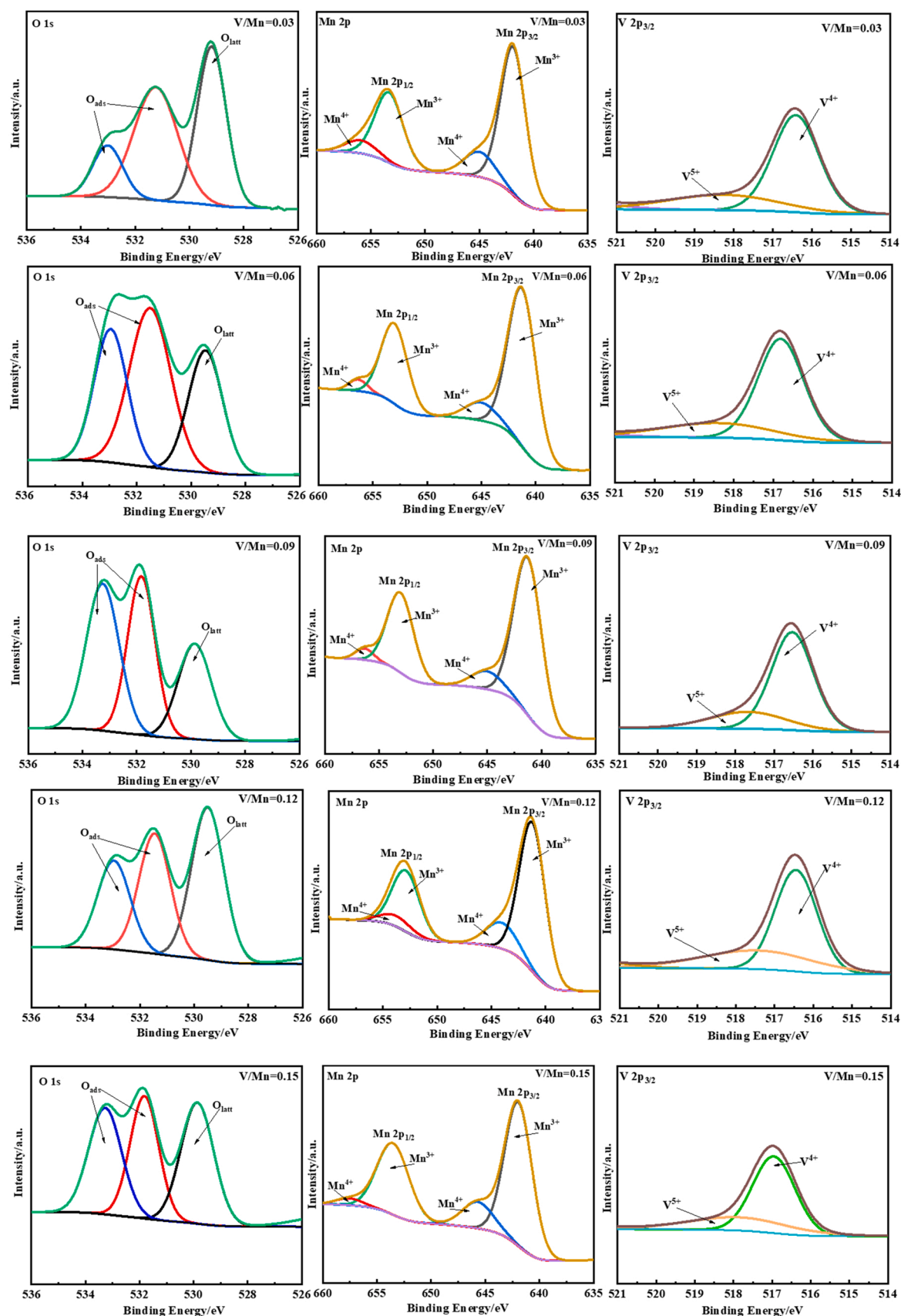


Fig. 2. O 1 s, Mn 2p and V 2p XPS spectra of catalysts prepared with multiple V/Mn molar ratios.

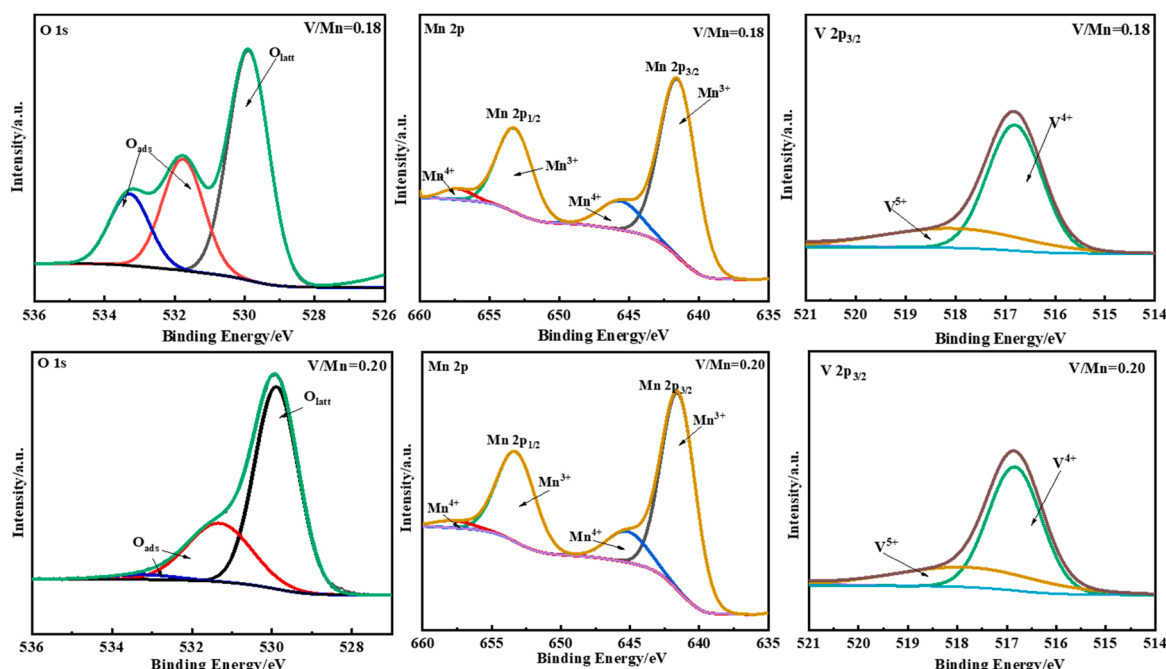


Fig. 2. (continued).

Table 2

XPS results of ϵ -MnO₂/Mn₂V₂O₇ prepared at different V/Mn molar ratios.

Catalysts (mole ratio)	HCHO degradation rate (%)	AOS	O _{ads} /O _{latt}	V ⁴⁺ /V ⁵⁺	Mn ³⁺ /Mn ⁴⁺
V/Mn = 0.03	37.0	2.93	1.41	2.62	4.86
V/Mn = 0.06	72.0	2.65	2.94	3.84	8.44
V/Mn = 0.09	69.3	2.82	2.91	3.31	5.67
V/Mn = 0.12	64.4	2.76	1.34	2.01	4.79
V/Mn = 0.15	63.5	2.71	2.33	2.37	6.11
V/Mn = 0.18	63.0	2.67	0.81	2.41	6.23
V/Mn = 0.20	62.3	2.67	0.46	2.29	6.62

preparation temperature for the catalyst.

Effect of the hydrothermal reaction time: A series of MnCO₃/Mn₂V₂O₇ precursors were synthesized while varying the hydrothermal time (1 h, 2 h, 3 h, 4 h, 5 h, and 6 h) at CO₂SM = 1.5 g, c(Mn²⁺) = 0.3 mol/L, V/Mn = 0.06 and T = 120 °C. The precursors were roasted at 320 °C for 6 h to obtain the corresponding catalysts as C-t₁, C-t₂, C-t₃, C-t₄, C-t₅, and C-t₆.

From Fig. S6(a), vanadium is shown to be well within the framework of ϵ -MnO₂. The hydrothermal time affects the strength of the Mn–O bond, and the characteristic peak at 647.4 cm^{−1} moves to 654.9 cm^{−1} when the hydrothermal time is extended from 1 h to 2 h, and to 621.8 cm^{−1} as the hydrothermal time increases to 6 h, as shown in Fig. S6(b). At t = 2 h, the short distance between both atoms results in a strong Mn–O bond and interaction between ϵ -MnO₂ and Mn₂V₂O₇, leading to the strongest catalytic oxidation performance. From Figs. S6 (c) and Fig. S6(d), the intensities of the precursor and composite catalyst diffraction peaks increase with the increasing hydrothermal time, and the crystallinity also increases. From Fig. S6(e), all samples are mesoporous, and the S_{BET} magnitudes follow the order t₂ > t₁ > t₃ > t₄ > t₅ > t₆. At t = 2 h, the catalyst formed has the largest S_{BET} (159.8 m²/g; Table S3), which corresponds with the HCHO degradation efficiency of the composite catalysts. From Fig. S7 and Table S4, the catalyst has the lowest average oxidation state at t = 2 h, implying that the presence of a large number of unsaturated Mn atoms in the catalyst structure that correspond to the maximum Mn³⁺/Mn⁴⁺, O_{ads}/O_{latt}, and V⁴⁺/V⁵⁺ ratios, demonstrate the presence of abundant oxygen vacancies and

adsorbed oxygen species. Therefore, the optimal preparation time for the catalyst is confirmed to be t = 2 h.

The effect of CO₂SM dosage: A series of MnCO₃/Mn₂V₂O₇ precursors were synthesized by varying the CO₂SM dosage (0.5 g, 1.0 g, 2.0 g, 2.5 g, and 3.0 g) at V/Mn = 0.06, c(Mn²⁺) = 0.3 mol/L, T = 120 °C and t = 2 h. The precursors were roasted at 320 °C for 6 h to obtain the corresponding catalysts as C-m_{0.5}, C-m_{1.0}, C-m_{1.5}, C-m_{2.0}, C-m_{2.5} and C-m_{3.0}.

Fig. S8(f) shows the effect of the CO₂SM dosage on ϵ -MnO₂/Mn₂V₂O₇ degradation of HCHO. The HCHO degradation ability of ϵ -MnO₂/Mn₂V₂O₇ increases between 0.5 and 1.5 g CO₂SM and decreases between 2.0 and 3.0 g CO₂SM; at CO₂SM = 1.5 g, the degradation efficiency reaches a maximum of 72.0%. Fig. S8(a) shows that vanadium successfully enters the ϵ -MnO₂ crystal framework and the adsorbed water molecules on the sample surface increase with increasing CO₂SM dosage. According to the Raman spectra (Fig. S8(b)), the characteristic peaks of the Mn–O bond are red-shifted and subsequently blue-shifted with an increase in the CO₂SM dosage, and the strongest effect of ϵ -MnO₂ and Mn₂V₂O₇ is observed at CO₂SM = 1.5 g. The characteristic peaks of V–O are not obvious or disappear when the CO₂SM dosage is between 2.0 and 3.0 g, proving that the content of Mn₂V₂O₇ in the composite catalyst is less and the synergistic catalytic ability is weakened. The S_{BET} values for the catalysts increase with increasing CO₂SM dosage (Fig. S8(e) and Table S5), which is attributed to the good dispersion ability of CO₂SM [64]. In addition, the surface properties of the catalysts are characterized using XPS at multiple CO₂SM dosages (Fig. S9 and Table S6). By split-peak fitting and quantitative analysis, a large amount of adsorbed oxygen species (O_{ads}/O_{latt} = 2.94), oxygen vacancies (Mn³⁺/Mn⁴⁺ = 8.44), and strong oxidation–reduction coupling ability (V⁴⁺/V⁵⁺ = 3.84) were present on the sample surface when CO₂SM = 1.5 g. Therefore, the optimum catalytic effect is achieved at CO₂SM = 1.5 g.

The effect of c(Mn²⁺): A series of MnCO₃/Mn₂V₂O₇ precursors were synthesized while varying the c(Mn²⁺) (0.15 mol/L, 0.20 mol/L, 0.25 mol/L, 0.30 mol/L, 0.35 mol/L, and 0.40 mol/L) at V/Mn = 0.06, CO₂SM = 1.5 g, T = 120 °C and t = 2 h. The precursors were roasted at 320 °C for 6 h to obtain the corresponding catalysts as C-c_{0.15}, C-c_{0.20}, C-c_{0.25}, C-c_{0.3}, C-c_{0.35}, and C-c_{0.40}.

Fig. S10(f) shows the effect of c(Mn²⁺) on the degradation of HCHO

by the ϵ -MnO₂/Mn₂V₂O₇ catalyst. When $c(\text{Mn}^{2+}) = 0.3 \text{ mol/L}$, ϵ -MnO₂/Mn₂V₂O₇ has the highest degradation efficiency for HCHO, with a value of 72.0%. The FTIR spectra (Fig. S10(a)), Raman spectra (Fig. S10(b)), XRD patterns (Fig. S10 (c) and (d)), N₂ adsorption-desorption isotherms (Fig. S10(e) and Table S7), and XPS characterization (Fig. S11 and Table S8), show that the catalyst has strong Mn–O bond, larger S_{BET} , and pore volume, abundant oxygen vacancies, and adsorbed surface oxygen species when $c(\text{Mn}^{2+}) = 0.3 \text{ mol/L}$ that is favorable for the catalytic oxidation reaction. Therefore, ϵ -MnO₂/Mn₂V₂O₇ exhibits the optimum catalytic performance at $c(\text{Mn}^{2+}) = 0.3 \text{ mol/L}$.

Based on the above results, V/Mn = 0.06, CO₂SM = 1.5 g, $c(\text{Mn}^{2+}) = 0.3 \text{ mol/L}$, $t = 2 \text{ h}$, and $T = 120^\circ\text{C}$ were the optimum preparation conditions for the precursors. The ϵ -MnO₂/Mn₂V₂O₇ catalyst made by roasting the precursor at 320°C for 6 h had the optimum HCHO degradation efficiency with a value of 72.0%.

Design of the response surface: To further optimize the influence of ϵ -MnO₂/Mn₂V₂O₇ preparation conditions on the efficiency of HCHO degradation, a response surface methodology (RSM) experimental design was performed [65]. Three influential factors (V/Mn molar ratio, CO₂SM dosage (g), and hydrothermal temperature ($^\circ\text{C}$)) were selected based on the single-factor experiments. Three factors at 3 levels are coded as shown in Table 3, and Box–Behnken experiments are designed as shown in Table 4 using the ϵ -MnO₂/Mn₂V₂O₇ degradation efficiency of HCHO as the response value. The experimental data are fitted to multiple models, and the optimal model is selected as shown in Table S9 and Fig. S12.

Surface response analysis: The analysis of variance (ANOVA) of ϵ -MnO₂/Mn₂V₂O₇ degradation rate of HCHO is shown in Table 5. Overall, $P = 0.0214 < 0.05$ and $R^2 = 0.8679$ indicate that the model is significant, suggesting that the quadratic polynomial model has a high degree of fit and confidence for HCHO degradation by ϵ -MnO₂/Mn₂V₂O₇. In Table 5, AB ($P = 0.0089 < 0.05$), AC ($P = 0.0209 < 0.05$), and A² ($P = 0.0060 < 0.05$) are significant models, indicating that these factors have a greater influence on the efficiency of HCHO degradation. The independent variables, A ($P = 0.0914 > 0.05$), B ($P = 0.4983 > 0.05$), C ($P = 0.4983 > 0.05$), BC ($P = 0.3107 > 0.05$), B² ($P = 0.1783 > 0.05$), and C² ($P = 0.6473 > 0.05$) were not significant, indicating that these factors did not significantly influence the degradation efficiency of HCHO.

Response surface and contour plots were obtained using the Design Expert 8.0.6 software to better visualize the effect of the interaction of any 2 factors on the degradation of HCHO by the ϵ -MnO₂/Mn₂V₂O₇ catalyst. The circular contours in the response surface plots indicate that the interaction between the parameters is not obvious, whereas contour lines, such as saddles or ellipses, indicate that the interaction between the parameters is stronger [66]. As shown in Fig. 3 and S13(a and b), the HCHO degradation efficiency arrived at an extreme HCHO degradation rate of 72.0% at V/Mn = 0.06, CO₂SM = 1.5 g, and $T = 120^\circ\text{C}$, which is consistent with the ANOVA results in Table 5.

Therefore, a quadratic polynomial model was determined to describe the effects of V/Mn molar ratio, CO₂SM dosage (g) and hydrothermal temperature ($^\circ\text{C}$) on the performance of ϵ -MnO₂/Mn₂V₂O₇ in degrading HCHO, as shown by the quadratic equation in Eq. (1):

$$\begin{aligned} \text{HCHO degradation rate} = & -127.53438 + 3425.83333 \text{ A} + 5.32500 \text{ B} + \\ & 1.36188 \text{ C} + 612.50000 \text{ AB} - 12.66667 \text{ AC} - 0.140000 \text{ BC} - \\ & 21569.44444 \text{ A}^2 - 7.56250 \text{ B}^2 - 1.49219 \times 10^{-3} \text{ C}^2 \end{aligned} \quad (1)$$

Table 3

Design factors and levels of the Box–Behnken experiment: A, V/Mn molar ratios; B, CO₂SM (g); and C, Hydrothermal temperatures ($^\circ\text{C}$).

Factors		Code values		
		-1	0	1
A	V/Mn	0.03	0.06	0.09
B	CO ₂ SM (g)	0.5	1.5	2.5
C	Temperature ($^\circ\text{C}$)	80	120	160

Table 4

Design and response of Box–Behnken experiment: A, V/Mn molar ratios; B, CO₂SM (g); and C, Hydrothermal temperatures ($^\circ\text{C}$).

Num	A	B	C	HCHO Degradation rate (%)
1	0.03	0.5	120	55.9
2	0.09	0.5	120	43.0
3	0.03	2.5	120	10.3
4	0.09	2.5	120	70.9
5	0.03	1.5	80	35.8
6	0.09	1.5	80	70.7
7	0.03	1.5	160	60.1
8	0.09	1.5	160	34.2
9	0.06	0.5	80	41.1
10	0.06	2.5	80	71.5
11	0.06	0.5	160	63.8
12	0.06	2.5	160	71.8
13	0.06	1.5	120	72.0
14	0.06	1.5	120	72.0
15	0.06	1.5	120	72.0
16	0.06	1.5	120	72.0
17	0.06	1.5	120	72.0

Table 5

Analysis of variance: A, V/Mn molar ratios; B, CO₂SM (g); and C, Hydrothermal temperatures ($^\circ\text{C}$).

Source	Sum of Squares	Df	Mean Square	F Value	p-value Prob > F	Significance
Model	4831.97	9	536.89	5.11	0.0214	**
A	410.86	1	401.86	3.82	0.0914	NS
B	53.56	1	53.56	0.51	0.4983	NS
C	14.58	1	14.58	0.14	0.7205	NS
AB	1350.56	1	1350.56	12.85	0.0089	**
AC	924.16	1	924.16	8.80	0.0209	**
BC	125.44	1	125.44	1.19	0.3107	NS
A ²	1586.72	1	1586.72	15.10	0.0060	**
B ²	240.81	1	240.81	2.29	0.1738	NS
C ²	24.00	1	24.00	0.23	0.6473	NS
Residual	735.49	7	105.07			
Lack of Fit	735.49	3	245.16			
Pure Error	0.000	4	0.000			
Cor Total	5567.46	16				

Note: (***) indicates highly significant ($p < 0.01$), ** indicates significant ($p < 0.05$), NS = not significant)

where A is the V/Mn molar ratio, B is the CO₂SM dosage (g), and C is the hydrothermal temperature ($^\circ\text{C}$).

According to single-factor and response surface experimental results, V/Mn = 0.06, CO₂SM = 1.5 g, $c(\text{Mn}^{2+}) = 0.3 \text{ mol/L}$, $t = 2 \text{ h}$, and $T = 120^\circ\text{C}$ were the optimum preparation conditions for the precursors. The ϵ -MnO₂/Mn₂V₂O₇ catalyst made by roasting the precursor at 320°C for 6 h had the optimum HCHO degradation efficiency with a value of 72.0%. The optimization results for the test conditions are shown in Fig. S14.

Most of the current studies on the catalytic oxidation of formaldehyde are focused on the gas phase, and not many studies on the catalytic oxidation of formaldehyde in the aqueous phase. The results of representative literature on the treatment of formaldehyde wastewater by CWAQ (Table 6) [10,11,67–69] were compared with the catalytic effect (ϵ -MnO₂/Mn₂V₂O₇) of this study, and the results are shown in Table 6. It can be seen that the reported catalysts for CWAQ treatment of formaldehyde wastewater generally have the problem of high reaction temperature, while the ϵ -MnO₂/Mn₂V₂O₇ catalyst prepared in this study showed excellent catalytic performance for low-temperature CWAQ treatment of formaldehyde wastewater. This indicates that the ϵ -MnO₂/Mn₂V₂O₇ catalyst has a great potential for application.

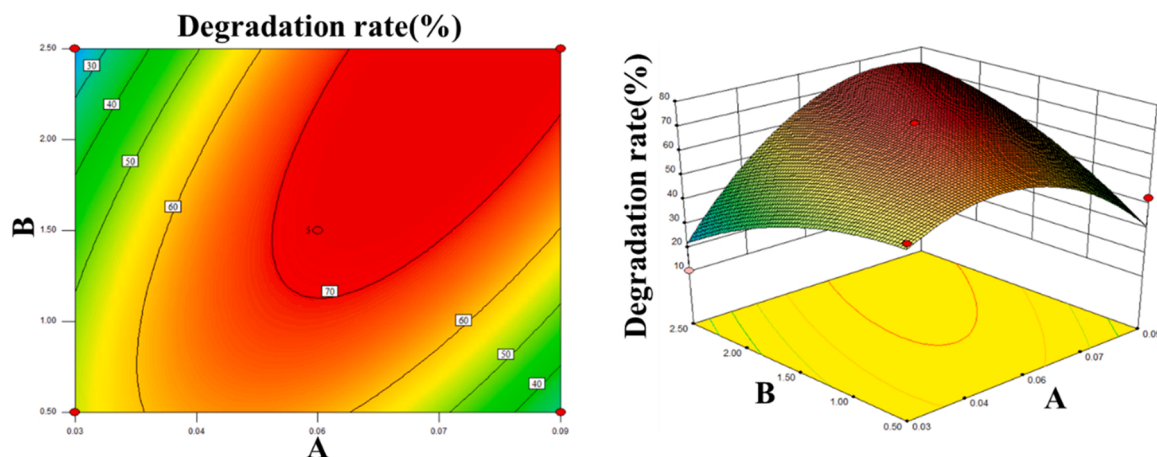


Fig. 3. Response surface and contour plots of the effect of the interaction of (A and B) on the degradation of HCHO by ϵ -MnO₂/Mn₂V₂O₇.

Table 6

Catalytic performance comparison of CWAQ catalysts for formaldehyde aqueous.

Catalysts	Reaction conditions	Conversion rate (%)	Ref
Pt/C-MnO ₂	40 mL, 800 ppm 50 °C, 2 MPa O ₂	88	[10]
Pt/C-MnO ₂	40 mL, 800 ppm 80 °C, 2 MPa O ₂	92	
Cu/TiO ₂	20 mL, 1000 mg/L 180 °C, 0.5 MPa O ₂	85	[67]
CuO-ZnO/Al ₂ O ₃	50 mL, 1500 ppm 160 °C, 1 MPa O ₂	80	[68]
Mn/Ce	50 mL, 1500 ppm 200 °C, 1.5 MPa O ₂	99	[69]
Pt-Bi-CeO ₂ /AC	30 mL, 12.40 mg/L 120 °C, 1.2 MPa Air	< 85	[11]
ϵ -MnO ₂ /Mn ₂ V ₂ O ₇	10 mL, 20 mg/L 30 °C, 0.1 MPa Air	72	This work

3.1.2. Formation mechanism for ϵ -MnO₂/Mn₂V₂O₇ composite catalyst

Based on the results shown in Fig. S15(a–c), a possible formation mechanism for the composite catalyst ϵ -MnO₂/Mn₂V₂O₇ is proposed (Fig. S15(d)). During the precursor formation process, the CO₂SM provides CO₃²⁻ and acts as a surfactant that plays a role in regulating crystal growth [70,71]. Initially, Mn²⁺ reacts with the CO₂SM and VO₄³⁻ to form the MnCO₃/Mn₂V₂O₇ complex, which may be due to competition between (Mn²⁺ + CO₂SM) and (Mn²⁺ + VO₄³⁻). Under hydrothermal conditions, the CO₂SM decomposes to release CO₂, 1,2-PDA, and 1,2-PPD, and the presence of 1,2-PDA makes the system alkaline, leading to the formation of CO₃²⁻ from CO₂ combined with H₂O with the simultaneous conversion of VO₄³⁻ to VO₃³⁻. Mn²⁺ and CO₃²⁻ preferentially combine to generate spherical MnCO₃ particles through 3 processes: nucleation, directed growth polymerization, and self-assembly. Small amounts of Mn²⁺ and VO₃³⁻ combine to form Mn(VO₃)₂ crystals with a rectangular-like structure. According to the literature [72], sodium lauryl sulfonate (SDS) and hydrothermal conditions play important roles in the formation of Mn₂V₂O₇ nanorods; therefore, it is presumed that CO₂SM influences the formation of Mn₂V₂O₇ nanosheets. The structures of 1,2-PDA and 1,2-PPD formed by the CO₂SM decomposition contain amine groups (-NH-) and (-OH) that are hydrophilic groups [73] and can provide coordination sites for positive ions to form structures, such as (1, 2-PDA-Mn²⁺ and 1,2-PPD-Mn²⁺). This leads to excessive local cation concentration, which attracts VO₃³⁻ until the formation of the Mn(VO₃)₂ nuclei. The electrostatic effect [74] causes 1,2-PDA and 1,2-PPD to adsorb on the surface of the Mn(VO₃)₂ nuclei, inducing the formation of Mn(VO₃)₂ crystals with a rectangular-like structure that aggregate and assemble to eventually form lamellar Mn₂V₂O₇. With an increase in

hydrothermal time and temperature, the flake structure grows and eventually forms the “layer-by-layer” Mn₂V₂O₇ phase. According to the literature [47,75], Mn²⁺ dissolved in MnCO₃ has a significant effect on the Mn₂V₂O₇ morphology, as shown in Eqs. (2) and (3). As the hydrothermal temperature increased, the concentration of Mn²⁺ from MnCO₃ dissolution increased, and Mn²⁺ could be randomly inserted into the lamellar structure of vanadium oxides, which is favorable for the growth of Mn₂V₂O₇ into a lamellar structure. Mn₂V₂O₇ crystals are relatively stable and their properties remain unchanged during calcination [72], resulting in the formation of ϵ -MnO₂/Mn₂V₂O₇ composite catalyst. In this process, there is a strong interaction between ϵ -MnO₂ and Mn₂V₂O₇, and V⁵⁺ enters the MnO₂ framework, replacing Mn⁴⁺ to inhibit MnO₂ crystal growth and increase the number of oxygen vacancies.



3.1.3. Stability

As shown in Fig. 4, the degradation efficiency of the ϵ -MnO₂/Mn₂V₂O₇ composite catalyst for HCHO tends to increase and subsequently decrease with an increase in the cycle number, but the degradation efficiency of ϵ -MnO₂/Mn₂V₂O₇ for HCHO still reaches above 67% after 5 cycles, proving that the catalyst has good stability. The slight increase in the degradation efficiency can be attributed to the increase in the number of cycles, the longer drying time of the sample, the increase

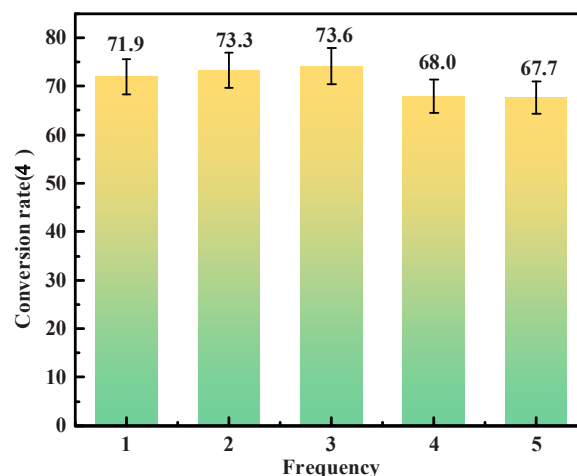


Fig. 4. Stability test of ϵ -MnO₂/Mn₂V₂O₇.

in the number of active sites, and the increase in the degradation efficiency. As the number of cycles continued to increase, the active sites on the surface were gradually occupied, and the degradation efficiency decreased.

3.2. Characterization of ϵ -MnO₂/Mn₂V₂O₇ and the synergistic catalytic mechanism

3.2.1. Characterization of ϵ -MnO₂/Mn₂V₂O₇

Scanning electron microscopy (SEM) and high-resolution transmission electron microscopy (HR-TEM) images: Fig. 5(a) shows the SEM images of ϵ -MnO₂ (A₁) and ϵ -MnO₂/Mn₂V₂O₇ (A₂). ϵ -MnO₂ (A₁) is composed of spherical particles with an average particle size of 1.42 μ m, and the surfaces of the spherical particles are aggregated with small nanoparticles. In the ϵ -MnO₂/Mn₂V₂O₇ (A₂) image, thin lamellar structures with a length of 864 nm and a width of 312 nm are generated on the surface of the MnO₂ particles and between gaps that can be related to the formation of Mn₂V₂O₇ in the composite catalyst, indicating that vanadium is successfully doped into the crystal phase of MnO₂. The grain size of the sample was calculated using the characteristic diffraction peaks of the MnO₂ (100) crystal plane, and the specific results are shown in Fig. 5(a). The inset of Fig. 5(a) shows that the average particle size of the composite catalyst (1.08 μ m) is lower than that of pure MnO₂ (1.42 μ m), indicating that V-doping hinders the growth of MnO₂ crystals and distorts the MnO₂ crystal structure.

To further investigate the microstructure and elemental distribution of ϵ -MnO₂/Mn₂V₂O₇, HR-TEM and energy-dispersive x-ray spectroscopy (EDS) mapping were performed. As shown in Fig. 5(b), Mn, O, and V are highly dispersed in the spherical particles (A–D), and the actual doping ratio (0.0587) is consistent with the theoretical doping ratio (0.06). As shown in Fig. 5(b) (E–I), lattice stripes with spacings of 0.15 nm, 0.25 nm, and 0.26 nm are attributed to the (424), (004), and (014)

crystal planes of Mn₂V₂O₇, while lattice stripes with spacings of 0.16 nm and 0.22 nm are assigned to the (102) and (002) crystal planes of ϵ -MnO₂. An HR-TEM image of ϵ -MnO₂ (Fig. S16) shows lattice stripes with a spacing of 0.28 nm assigned to the (100) crystal plane of ϵ -MnO₂ that shows that after V-doping, the sample exposes more high index crystal planes, which usually have more active sites. This implies the presence of more unsaturated atoms in the ϵ -MnO₂/Mn₂V₂O₇ structure, which favors catalytic reactions [45,76,77]. In addition, V-doping causes the lattice stripe to become disordered and blurred [78], where the distortion of MnO structure is caused by high levels of doped species. Mizuno et al. [79] found that V⁵⁺ inhibits the growth of α -MnO₂ along the c-axis. Therefore, it is speculated that V⁵⁺ replaces Mn⁴⁺ in the formation of ϵ -MnO₂/Mn₂V₂O₇, inhibiting the growth of MnO₂ crystals. Meanwhile, grain boundaries are formed between MnO₂ and Mn₂V₂O₇, and the presence of more unsaturated atoms and oxygen vacancies on the grain boundary surface helps improve oxygen migration and activation [80]; thus, the catalytic activity of ϵ -MnO₂/Mn₂V₂O₇ is higher than that of ϵ -MnO₂.

Hydrogen-temperature programmed reduction (H₂-TPR): The redox properties of the catalysts were studied using H₂-TPR. From Fig. 5(c), the H₂-TPR curve of ϵ -MnO₂ (C-0) consists of 4 peaks α (301.5 °C), β (329.3 °C), γ (416.2 °C), and η (449.8 °C). The α peak is attributed to the reduction of oxygen adsorbed onto the surface of MnO₂ crystals, whereas β , γ , and η peaks correspond to the successive reduction of MnO₂ itself as MnO₂ → Mn₂O₃ → Mn₃O₄ → MnO [81]. With V-doping, the shape of the reduction curve of the composite catalyst, ϵ -MnO₂/Mn₂V₂O₇ (C-0.06), becomes “flat” because V-doping destroys the crystal structure of MnO₂ and forms a large number of vacancies [82]. Concurrently, the reduction peak of adsorbed oxygen on the surface of MnO₂ crystals (α -peak) decreases to 286.7 °C, and the interaction between ϵ -MnO₂ and Mn₂V₂O₇ generates several surface oxygen vacancies, more O_{ads} species, and the mobility of O_{latt}. Therefore, the

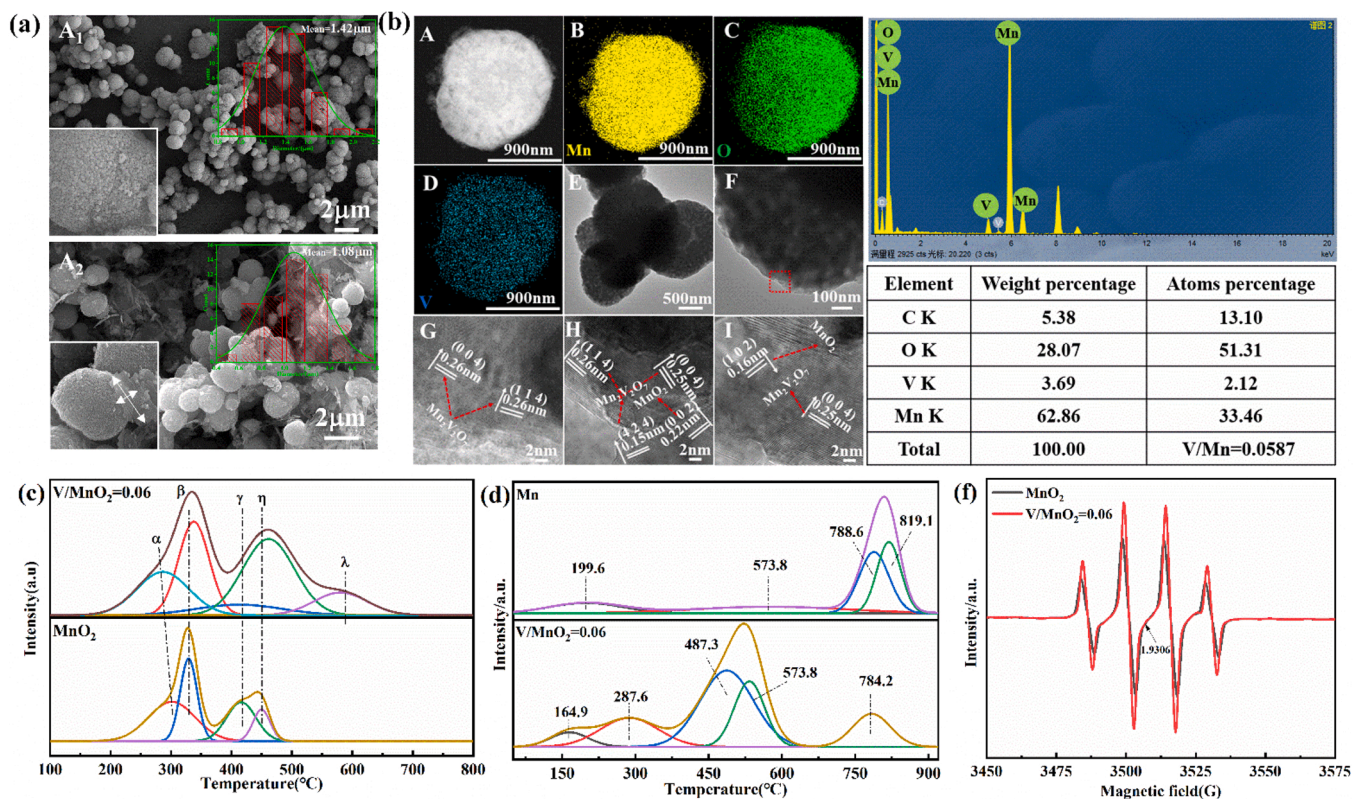


Fig. 5. SEM images, H₂-TPR curves, O₂-TPD curves, EPR curves of C-0 and C-0.06, and HR-TEM images of C-0.06. (a) A₁ is the SEM image of C-0, A₂ is the SEM image of C-0.06, (b) A is the SEM image of C-0.06; B, C, and D are the mapping results of Mn, O, and V elements, respectively; E and F are the TEM images of catalyst; G, H, and I are the enlarged images in box F, (c) H₂-TPR curves of C-0 and C-0.06, (d) O₂-TPD curves of C-0 and C-0.06, (e) EPR curves of C-0 and C-0.06.

active oxygen is transferred to a lower temperature for reduction [82]. In the 500–600 °C range, another broad reduction λ (580.3 °C) peak is detected for the composite catalyst, ϵ -MnO₂/Mn₂V₂O₇ (C-0.06) that can be attributed to the reduction of V⁵⁺ by the strong interaction of Mn₂V₂O₇ with MnO₂ [83]. The total H₂ consumption of ϵ -MnO₂ (C-0) is 1.62 mmol/g, while the total H₂ consumption of the composite catalyst ϵ -MnO₂/Mn₂V₂O₇ (C-0.06) is 1.73 mmol/g that is attributed to the large production of V⁵⁺ which increases the total H₂ consumption of the composite catalyst.

Temperature-programmed desorption of oxygen (O₂-TPD): The oxygen species and mobility of the catalysts were studied using O₂-TPD. Generally, oxygen desorption curves can be divided into 3 parts: less than 300 °C, between 300 and 650 °C, and greater than 650 °C, corresponding to surface adsorbed oxygen molecules and active oxygen species, subsurface lattice oxygen, and bulk phase lattice oxygen, respectively [84]. As shown in Fig. 5(d), there is an increase in adsorbed oxygen species on the surface of ϵ -MnO₂/Mn₂V₂O₇ (C-0.06) compared with ϵ -MnO₂ (C-0) which is attributed to V-doping and leads to the generation of a large number of oxygen vacancies. Furthermore, the adsorption of oxygen molecules to oxygen vacancies generates a large number of adsorbed oxygen species that can be desorbed at lower temperatures [84]. The desorption peak located between 300 and 650 °C shifts toward a lower temperature (487.3 °C) with V-doping, indicating that the otherwise stable lattice oxygen species in ϵ -MnO₂/Mn₂V₂O₇ (C-0.06) are more mobile and easily activated to participate in the reaction when in contact with HCHO molecules [85, 86]. In addition, the desorption of surface lattice oxygen in the range of 300–650 °C is generally accompanied by the reduction of Mn³⁺ in the Mn⁴⁺ phase and the generation of synergistic V⁴⁺-□-Mn³⁺ oxygen vacancies. As shown in Fig. 5(d), the area of the desorption peak increases

significantly for the ϵ -MnO₂/Mn₂V₂O₇ (C-0.06) catalyst while oxygen molecules are usually adsorbed at the oxygen vacancy sites. ϵ -MnO₂/Mn₂V₂O₇ (C-0.06) contains a large number of oxygen vacancies, which favors the catalytic reaction.

Electron paramagnetic resonance (EPR): To determine the reactive oxygen species (ROS) on the catalyst surface, EPR technology was used to study both ϵ -MnO₂ (C-0) and ϵ -MnO₂/Mn₂V₂O₇ (C-0.06) catalysts using 5, 5-dimethyl-1-pyrroline N-oxide (DMPO) as a radical trapping agent. As shown in Fig. 5(f), EPR signals are observed at the same position for both ϵ -MnO₂ and ϵ -MnO₂/Mn₂V₂O₇ catalysts, and both have 4 characteristic peaks. According to the literature [87], superoxide ($\cdot\text{O}_2^-$), monoclinic oxide ($^1\text{O}_2$), and H₂O₂ cannot oxidize DMPO to DMPO-X, but hydroxyl radicals ($\cdot\text{OH}$) combine with DMPO to generate DMPO- $\cdot\text{OH}$ -adducts and a quadruple signal peak with 1:2:2:1 intensity. This proves that the surfaces of ϵ -MnO₂ and ϵ -MnO₂/Mn₂V₂O₇ catalysts contain a large number of $\cdot\text{OH}$ radicals that play a key role in the catalytic oxidation of HCHO [87]. The EPR signal of ϵ -MnO₂/Mn₂V₂O₇ in Fig. 5(f) is significantly stronger than that of ϵ -MnO₂, indicating that the catalytic oxidation performance is enhanced by the increase in ROS on the catalyst surface after V-doping.

Combined with the results above, V-doping causes the catalyst structure to produce a thin lamellar Mn₂V₂O₇ structure, and there may be grain boundaries between them that promote the generation of oxygen vacancies in large quantities, providing a basis for synergistic catalysis. V-doping inhibits the growth of MnO₂ crystals, decreasing the crystallinity of the sample and increasing the content of adsorbed oxygen and oxygen vacancies, which leads to the excellent catalytic performance of ϵ -MnO₂/Mn₂V₂O₇.

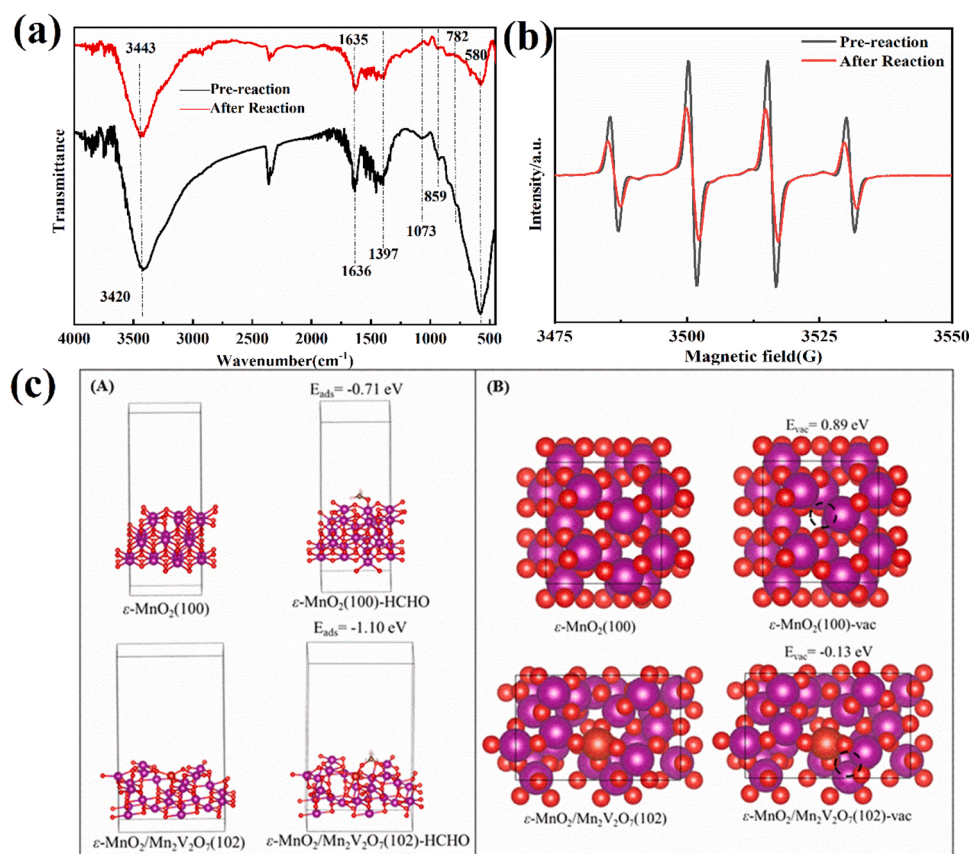


Fig. 6. (a) FTIR spectra of ϵ -MnO₂/Mn₂V₂O₇ before and after HCHO degradation at 30 °C and 500 rpm, (b) EPR curves of ϵ -MnO₂/Mn₂V₂O₇ before and after HCHO degradation at 30 °C and 500 rpm and (c).

(A) HCHO adsorption energy and (B) formation energy of oxygen vacancy.

3.2.2. Synergistic catalytic mechanism of ϵ -MnO₂/Mn₂V₂O₇

As shown in Fig. 6(a), the characteristic peaks of the samples hardly changed after the reaction, indicating that the basic properties of ϵ -MnO₂/Mn₂V₂O₇ did not change during the reaction. According to the literature [85], -OH is crucial for the HCHO-catalyzed oxidation reaction. The telescopic vibration of -OH located at 3443 cm⁻¹ decreases in intensity after the reaction, proving that -OH is involved in the catalytic oxidation process. The stretching vibration of the Mn-O bond located at 580 cm⁻¹ also decreases in intensity after the reaction, indicating that the Mn-O bond plays a key role in the catalytic oxidation process. As shown in Fig. 6(b), the -OH free radical signal on the sample surface weakens after the reaction. In addition, the degradation of HCHO by ϵ -MnO₂/Mn₂V₂O₇ was tested under light and dark conditions, and the specific results are shown in Fig. S17. The difference in degradation rate between light and dark reactions is 3.24% as seen in the figure. Therefore, it can be presumed that the photocatalytic process is weak in this reaction, and the main effect is thermal catalysis.

As shown by the TEM images, the (100) and (102) crystal planes are exposed to ϵ -MnO₂ before and after V-doping, respectively; therefore, both crystal planes are selected to build the surface model. The equilibrium lattice constants of the ϵ -MnO₂ unit cell were optimized as $a = b = 2.786$ Å and $c = 4.412$ Å. Two surface models were constructed. The first was a MnO₂ (100) surface with $p(3 \times 2)$ periodicity in the X and Y directions and 3 stoichiometric layers in the z-direction by a vacuum depth of 15 Å to separate the surface slab from its periodic duplicates. During structural optimization, a $3 \times 3 \times 1$ k-point grid in the Brillouin zone was used for k-point sampling, and the bottom 2 stoichiometric layers were fixed, while the rest were allowed to relax fully. The second was a V-doped MnO₂ (102) surface model with $p(2 \times 3)$ periodicity in the x and y directions and 4 stoichiometric layers in the z-direction by a vacuum depth of 15 Å was used to separate the surface slab from its periodic duplicates. During structural optimizations, a $2 \times 3 \times 1$ k-point grid in the Brillouin zone was used for k-point sampling, and the bottom 2 stoichiometric layers were fixed, while the rest were allowed to relax fully.

As shown in Fig. 6(c-A), the adsorption energy of HCHO in pure ϵ -MnO₂ is -0.71 eV that changes to -1.10 eV after doping with vanadium, proving that HCHO molecules are more easily adsorbed onto the surface of ϵ -MnO₂/Mn₂V₂O₇ crystals. Fig. 6(c-B) shows that the energy required to form an oxygen vacancy is 0.89 eV for pure ϵ -MnO₂ and -0.13 eV for the formation of oxygen vacancy after doping with vanadium. Generally, the lower the energy for the formation of an oxygen vacancy, the easier it is to form oxygen vacancies. This result indicates that doping with high-valent vanadium is more likely to generate oxygen vacancies with content closely related to the catalytic oxidation activity of HCHO; therefore, the catalytic oxidation activity is increased significantly after doping with vanadium. In addition, to further

evaluate the oxygen vacancy density before and after doping, electron paramagnetic resonance tests were performed (Fig. S18), and it was found that the EPR signal of the sample was enhanced after V doping, demonstrating the increased oxygen vacancy content on the surface and thus the enhanced catalytic oxidation capacity.

Combining the above results with the relevant literature [85,86], the synergistic catalytic mechanism for the composite catalyst ϵ -MnO₂/Mn₂V₂O₇ is proposed (Fig. 7). V-doping inhibits the growth of MnO₂ crystals, reduces their crystallinity, and increases their specific surface area, thereby exposing more oxygen vacancies. From the XRD, XPS, and HR-TEM results, vanadium is uniformly distributed in the ϵ -MnO₂ main phase and successfully synthesized into Mn₂V₂O₇ crystals. Grain boundaries are formed between them where more unsaturated atoms and oxygen vacancies exist; thus, more ROS can be adsorbed, favoring the catalytic reaction.

At the beginning of the reaction, HCHO molecules in an aqueous solution are adsorbed on the -OH group of ϵ -MnO₂/Mn₂V₂O₇ by hydrogen bonding, whereas O₂ molecules in solution are adsorbed and dissociated into oxygen vacancies, achieving O₂ molecular activation to form ROS (O*), favoring the subsequent oxidation of HCHO (Step I) [88]. The electron cloud in the HCHO molecule is biased toward the O atom, making the carbonyl carbon atom somewhat electrophilic and susceptible to attack by nucleophilic oxygen species to generate dioxymethylene (DOM) (Step II) [89]. DOM is rapidly oxidized by ROS (O*) and converted to formate (Step III) [88]. Thereafter, the -OH group on the sample surface rapidly converted formate to unstable carbonic acid that dissociated rapidly into CO₂ and H₂O which was removed from the catalyst surface, and the catalyst returned to its original state (Step IV). In this process, -OH groups are derived from the adsorbed water onto the sample and generated by the activation of O₂ molecules and water (and/or reaction products) through a large number of oxygen vacancies (Step V) [88]. Compared with pure MnO₂, ϵ -MnO₂/Mn₂V₂O₇ contains more oxygen vacancies on its surface that can continuously activate O₂ molecules and produce more -OH groups. According to the literature [89], the conversion of formate is the decisive step in the overall catalytic reaction, and more -OH groups imply a faster reaction rate; thus, ϵ -MnO₂/Mn₂V₂O₇ has an excellent HCHO degradation ability.

4. Conclusion

MnCO₃/Mn₂V₂O₇ precursors were prepared by a hydrothermal reaction using Mn²⁺, CO₂SM, and vanadate as raw materials without additional template agents and surfactants, and further roasted to synthesize ϵ -MnO₂/Mn₂V₂O₇ composite catalysts. At 30 °C, 500 rpm, the HCHO degradation rate of Mn (VO₃)₂ was 25.2% and that of ϵ -MnO₂ was 35.7%, while that of the ϵ -MnO₂/Mn₂V₂O₇ composite catalyst was up to 72.0%, indicating a strong synergistic catalytic ability. The substitution

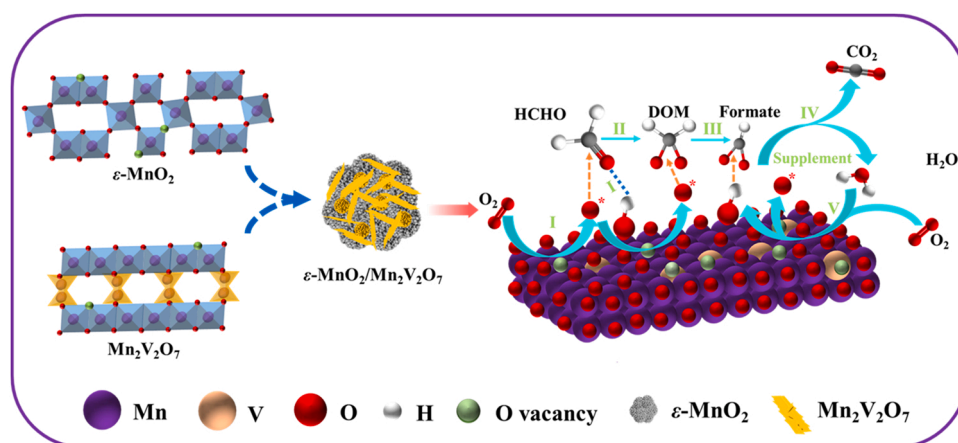


Fig. 7. ϵ -MnO₂/Mn₂V₂O₇ synergistic catalytic mechanism.

of V^{5+} for Mn^{4+} in the process of V-doping distorted the MnO_2 crystal structure, the low chemical state of Mn, and the high-index crystal plane (100), resulting in more oxygen vacancies. Grain boundaries were easily generated between ϵ - MnO_2 and $Mn_2V_2O_7$, leading to a large number of oxygen vacancies and adsorption of more active oxygen species onto the surface of the composite catalyst. The degradation rate of 20 mg/L 10 mL HCHO solution reached 72.0% at 30 °C for 1 h, and the degradation rate remained above 67.0% after 5 cycles on the ϵ - MnO_2 / $Mn_2V_2O_7$ composite catalyst prepared at $V/Mn = 0.06$ and $T = 120$ °C.

CRedit authorship contribution statement

Xuang Liu and Jialin Wu: Investigation, Writing – original draft. **Shuai Zhang:** Investigation. **Qiang Li:** Data curation, Methodology. **Zhaojun Wu:** Project administration, Methodology. **Jianbin Zhang:** Data curation, Project administration, Funding acquisition, Methodology, Writing – review & editing.

Declaration of Competing Interest

The authors declare that they have no known competing financial interests or personal relationships that could have appeared to influence the work reported in this paper.

Data Availability

Data will be made available on request.

Acknowledgements

This work was supported by the Program for Grassland Excellent Talents of Inner Mongolia Autonomous Region, the Inner Mongolia Science and Technology Key Projects, and Beijing Boyuan Hengsheng High-Tech. Co., Ltd., Beijing, China (HA2157).

Supporting Information

The supplementary information involves 9 Tables and 18 Figures, including the preparation process of CO_2SM and related characterization; HCHO standard curve; characterization of catalyst FTIR, Raman, XRD, BET, XPS and performance prepared at different hydrothermal temperatures; characterization of catalyst FTIR, Raman, XRD, BET, XPS and performance prepared at different hydrothermal times; characterization of catalyst FTIR, Raman, XRD, BET, XPS and performance prepared at different CO_2SM dosages; characterization of catalyst FTIR, Raman, XRD, BET, XPS and performance prepared at different $c(Mn^{2+})$; optimization of response surface model selection methods, residual data, contour plots, and reaction conditions; HR-TEM images of pure MnO_2 images; schematic diagram of the formation mechanism of ϵ - MnO_2 / $Mn_2V_2O_7$ composite catalyst; light and dark reaction processes of ϵ - MnO_2 / $Mn_2V_2O_7$; and EPR Curve.

Appendix A. Supporting information

Supplementary data associated with this article can be found in the online version at [doi:10.1016/j.apcatb.2022.121994](https://doi.org/10.1016/j.apcatb.2022.121994).

References

- [1] T. Salthammer, S. Mentese, R. Marutzky, Formaldehyde in the indoor environment, *Chem. Rev.* 110 (2010) 2536–2572.
- [2] J.Q. Torres, S. Royer, J.P. Bellat, J.M. Giraudon, J.F. Lamonier, Formaldehyde: catalytic oxidation as a promising soft way of elimination, *ChemSusChem* 6 (2013) 578–592.
- [3] H.R. Lotfy, I.G. Rashed, A method for treating wastewater containing formaldehyde, *Water Res* 36 (2002) 633–637.
- [4] M. Delikhoon, M. Fazlzadeh, A. Sorooshian, A.H. Baghani, M. Golaki, Q. Ashournejad, A. Barkhordari, Characteristics and health effects of formaldehyde and acetaldehyde in an urban area in Iran, *Environ. Pollut.* 242 (2018) 938–951.
- [5] M.M. Wang, B.M. Fan, B.Y. Wen, J. Chao, Experimental and theoretical studies on the removal mechanism of formaldehyde from water by mesoporous calcium silicate, *Sci. China Technol. Sc.* 63 (2020) 2098–2122.
- [6] Y. Zvulunov, Z. Ben-Barak-Zelas, A. Fishman, A. Radian, A self-regenerating clay-polymer-bacteria composite for formaldehyde, *Chem. Eng. J.* 374 (2019) 1275–1285.
- [7] Z. Pásztor, K. Halász, Z. Börcsök, Formaldehyde adsorption-desorption of poplar bark, *Bull. Environ. Contam. Toxicol.* 103 (2019) 745–749.
- [8] P. Kajitvichyanukul, M.C. Lu, C.H. Liao, W. Wirojanagud, T. Koottatep, Degradation and detoxification of formaline wastewater by advanced oxidation processes, *J. Hazard. Mater.* 135 (2006) 337–343.
- [9] L. Du, P. Li, W. Gao, X. Ding, W. Jiao, Y. Liu, Enhancement degradation of formaldehyde by $MgO/\gamma-Al_2O_3$ catalyzed O_3/H_2O_2 a rotating packed bed, *J. Taiwan. Inst. Chem. E* 118 (2021) 29–37.
- [10] L. Geng, C. Rong, A. Lin, H. Shi, M. Zhang, N. Zhang, B. Chen, Low temperature high efficiency catalytic wet oxidation Pt/ MnO_2 catalyst for formaldehyde wastewater treatment, *Chinese. Sci. Bull.* 22 (2021) 2898–2907.
- [11] R.C. Wei, H.L. Chen, X.M. Zhang, Treatment of glyphosate wastewater with high concentration of formaldehyde by wet catalytic oxidation, *J. Mol. Catal.* 27 (2013) 323–332.
- [12] M. Miao, J. Ji, B. Liu, H. Huang, Reduced TiO_2 with tunable oxygen vacancies for catalytic oxidation of formaldehyde at room temperature, *Appl. Surf. Sci.* 473 (2019) 934–942.
- [13] M. Sun, X. Wang, Z. Chen, M. Murugananthan, Y. Chen, Y. Zhang, Stabilized oxygen vacancies over heterojunction for highly efficient and exceptionally durable VOCs photocatalytic degradation, *Appl. Catal. B Environ.* 273 (2020), 119061.
- [14] H. Pan, M. Sun, X. Wang, M. Zhang, M. Murugananthan, Y. Zhang, A novel electric-assisted photocatalytic technique using self-doped TiO_2 nanotube films, *Appl. Catal. B Environ.* 307 (2022), 121174.
- [15] M. Sun, X. Wang, Y. Li, H. Pan, M. Murugananthan, Y. Han, J. Wu, M. Zhang, Y. Zhang, Z. Kang, Bifunctional $Pd-O_x$ center at the liquid–solid–gas triphase interface for H_2O_2 photosynthesis, *ACS Catal.* 12 (2022) 2138–2149.
- [16] Z. Wang, W. Wang, L. Zhang, D. Jiang, Surface oxygen vacancies over Co_3O_4 mediated catalytic formaldehyde oxidation at room temperature, *Catal. Sci. Technol.* 00 (2012) 1–3.
- [17] B. Bai, Q. Qiao, J. Li, J. Hao, Synthesis of three-dimensional ordered mesoporous MnO_2 and its catalytic performance in formaldehyde oxidation, *Chinese. J. Catal.* 37 (2016) 27–31.
- [18] S. Lu, K. Li, F. Huang, C. Chen, B. Sun, Efficient $MnO_x-Co_3O_4-CeO_2$ catalysts for formaldehyde elimination, *Appl. Surf. Sci.* 400 (2017) 277–282.
- [19] Y. Sekine, Oxidative decomposition of formaldehyde by metal oxides at room temperature, *Atmos. Environ.* 36 (2002) 5543–5547.
- [20] J. Zhang, Y. Li, L. Wang, C. Zhang, H. He, Catalytic oxidation of formaldehyde over manganese oxides with different crystal structures, *Catal. Sci. Technol.* 5 (2015) 2305–2313.
- [21] Y. Gao, H. Huang, W. Tang, X. Liu, X. Yang, J. Zhang, Preparation and characterization of a novel porous silicate material from coal gangue, *Microporous Mesoporous Mater.* 217 (2015) 210–218.
- [22] K. Liu, B. Zhao, Y. Wu, F. Li, Q. Li, J. Zhang, Bubbling synthesis and high-temperature CO_2 adsorption performance of CaO -based adsorbents from carbide slag, *Fuel* 269 (2020), 117481.
- [23] W. Tang, H. Huang, Y. Gao, X. Liu, X. Yang, H. Ni, J. Zhang, Preparation of a novel porous adsorption material from coal slag and its adsorption properties of phenol from aqueous solution, *Mater. Des.* 88 (2015) 1191–1200.
- [24] P. Liu, H. He, G. Wei, X. Liang, F. Qi, F. Tan, W. Tan, J. Zhu, R. Zhu, Effect of Mn substitution on the promoted formaldehyde oxidation over spinel ferrite: Catalyst characterization, performance and reaction mechanism, *Appl. Catal. B Environ.* 182 (2016) 476–484.
- [25] Y. Wen, X. Tang, J. Li, J. Hao, L. Wei, X. Tang, Impact of synthesis method on catalytic performance of MnO_x-SnO_2 for controlling formaldehyde emission, *Catal. Commun.* 10 (2009) 1157–1160.
- [26] J. Pei, H. Xu, L. Yi, Performance and kinetics of catalytic oxidation of formaldehyde over copper manganese oxide catalyst, *Build. Environ.* 84 (2015) 134–141.
- [27] X. Tang, Y. Li, X. Huang, Y. Xu, H. Zhu, J. Wang, W. Shen, MnO_x-CeO_2 mixed oxide catalysts for complete oxidation of formaldehyde: Effect of preparation method and calcination temperature, *Appl. Catal. B Environ.* 62 (2006) 265–273.
- [28] D. Li, G. Yang, P. Li, J. Wang, P. Zhang, Promotion of formaldehyde oxidation over Ag catalyst by Fe doped MnO_x support at room temperature, *Catal. Today* 277 (2016) 257–265.
- [29] Z. Fan, Z. Zhang, W. Fang, X. Yao, G. Zou, W. Shang, Low-temperature catalytic oxidation of formaldehyde over Co_3O_4 catalysts prepared using various precipitants, *Chinese. J. Catal.* 37 (2016) 947–954.
- [30] J. Ma, C. Wang, H. He, Transition metal doped cryptomelane-type manganese oxide catalysts for ozone decomposition, *Appl. Catal. B-Environ.* 201 (2017) 503–510.
- [31] X. Du, C. Li, L. Zhao, J. Zhang, L. Gao, J. Sheng, Y. Yi, J. Chen, G. Zeng, Promotional removal of HCHO from simulated flue gas over Mn-Fe oxides modified activated coke, *Appl. Catal. B Environ.* 232 (2018) 37–48.
- [32] Y. Yang, P. Zhang, J. Jia, Vanadium-doped MnO_2 for efficient room-temperature catalytic decomposition of ozone in air, *Appl. Surf. Sci.* 484 (2019) 45–53.
- [33] M. Polverejan, J.C. Villegas, S.L. Suib, Higher valency ion substitution into the manganese oxide framework, *J. Am. Chem. Soc.* 126 (2004) 7774–7775.

- [34] N. Agmon, Isoelectronic theory for cationic radii, *J. Am. Chem. Soc.* 139 (2017) 15068–15073.
- [35] F. Li, J. Wu, Q. Qin, Z. Li, X. Huang, Facile synthesis of γ -MnOOH micro/nanorods and their conversion to β -MnO₂, *Mn₃O₄*, *J. Alloy. Compd.* 492 (2010) 339–346.
- [36] E. Eren, H. Gumus, A. Sarihan, Synthesis, structural characterization and Pb (II) adsorption behavior of K- and H-birnessite samples, *Desalination* 279 (2011) 75–85.
- [37] V. Dimitrov, Structural changes in vitreous vanadate systems, *J. Non Cryst. Solids* 193 (1995) 183–186.
- [38] O. Yamaguchi, Y. Mukaida, H. Shigeta, H. Takemura, M. Yamashita, Preparation of alkoxy-derived YVO₄, *Mater. Lett.* 7 (1988) 158–160.
- [39] T. Gao, H. Fjellvag, P. Norby, A comparison study on Raman scattering properties of α - and β -MnO₂, *Anal. Chim. Acta* 648 (2009) 235–239.
- [40] J. Liu, Y.C. Son, J. Cai, X. Shen, S.L. Suib, M. Aindow, Size control, metal substitution, and catalytic application of cryptomelane nanomaterials prepared using cross-linking reagents, *Chem. Mater.* 16 (2004) 276–285.
- [41] H.C. Genuino, Y. Meng, D.T. Horvath, C.H. Kou, M.S. Seraji, A.M. Morey, R. L. Joesten, S.L. Suib, Enhancement of catalytic activities of octahedral molecular sieve manganese oxide for total and preferential CO oxidation through vanadium ion framework substitution, *ChemCatChem* 5 (2013) 2306–2317.
- [42] L. Sun, Q. Cao, B. Hu, J. Li, J. Hao, G. Jing, X. Tang, Synthesis, characterization and catalytic activities of vanadium-cryptomelane manganese oxides in low-temperature NO reduction with NH₃, *Appl. Catal. A Gen.* 393 (2011) 323–330.
- [43] X. Tang, J. Li, J. Hao, Significant enhancement of catalytic activities of manganese oxide octahedral molecular sieve by marginal amount of doping vanadium, *Catal. Commun.* 11 (2010) 871–875.
- [44] J. Chen, X. Chen, W. Xu, Z. Xu, J. Chen, H. Jia, J. Chen, Hydrolysis driving redox reaction to synthesize Mn-Fe binary oxides as highly active catalysts for the removal of toluene, *Chem. Eng. J.* 330 (2017) 281–293.
- [45] S. Rong, P. Zhang, F. Liu, Y. Yang, Engineering crystal facet of α -MnO₂ nanowire for highly efficient catalytic oxidation of carcinogenic airborne formaldehyde, *ACS Catal.* 8 (2018) 3435–3446.
- [46] T. Li, C. Guo, S. Bo, T. Li, Y. Li, L. Hou, Y. Wei, Well-shaped Mn₃O₄ tetragonal bipyramids with good performance for lithium-ion batteries, *J. Mater. Chem. A* 3 (2015) 7248–7254.
- [47] Y. Liu, Y.P. Zeng, Controllable synthesis of β -Mn₂V₂O₇ microtubes and hollow microspheres, *Mater. Lett.* 63 (2009) 28–30.
- [48] R. Li, Y. Huang, D. Zhu, W. Ho, J. Cao, S. Lee, Improved oxygen activation over a carbon/Co₃O₄ nanocomposite for efficient catalytic oxidation of formaldehyde at room temperature, *Environ. Sci. Technol.* 55 (2021) 4054–4063.
- [49] K. Zha, W. Sun, Z. Huang, H. Xu, W. Shen, Insights into high-performance monolith catalysts of Co₃O₄ nanowires grown on nickel foam with abundant oxygen vacancies for formaldehyde oxidation, *ACS Catal.* 10 (2020) 12127–12138.
- [50] A. Rutger, V. Santen, Complementary structure sensitive and insensitive catalytic relationships, *Acc. Chem. Res.* 42 (2009) 57–66.
- [51] T. Ge, Z. Jiang, L. Shen, J. Li, Z. Lu, Y. Zhang, F. Wang, Synthesis and application of Fe₃O₄/FeWO₄ composite as an efficient and magnetically recoverable visible light-driven photocatalyst for the reduction of Cr(VI), *Sep. Purif. Technol.* 263 (2021), 118401.
- [52] J. Li, T. Peng, Y. Zhang, C. Zhou, A. Zhu, Polyaniline modified SnO₂ nanoparticles for efficient photocatalytic reduction of aqueous Cr(VI) under visible light, *Sep. Purif. Technol.* 201 (2018) 120–129.
- [53] S. Xie, J. Deng, Y. Liu, Z. Zhang, H. Yang, Y. Jiang, H. Arandiyana, H. Dai, C.T. Au, Excellent catalytic performance, thermal stability, and water resistance of 3DOM Mn₂O₃-supported Au-Pd alloy nanoparticles for the complete oxidation of toluene, *Appl. Catal. A Gen.* 507 (2015) 82–90.
- [54] J. Jia, W. Yang, P. Zhang, J. Zhang, Facile synthesis of Fe-modified manganese oxide with high content of oxygen vacancies for efficient airborne ozone destruction, *Appl. Catal. A Gen.* 546 (2017) 79–86.
- [55] J. Jia, P. Zhang, L. Chen, Catalytic decomposition of gaseous ozone over manganese dioxides with different crystal structures, *Appl. Catal. B-Environ.* 189 (2016) 210–218.
- [56] Z. Lin, J. Wang, S. Rong, H. Wang, P. Zhang, Cerium modified birnessite-type MnO₂ for gaseous formaldehyde oxidation at low temperature, *Appl. Catal. B-Environ.* 211 (2017) 212–221.
- [57] V.P. Santos, M. Pereira, J.J.M. Orfao, J.L. Figueiredo, Catalytic oxidation of ethyl acetate over a cesium modified cryptomelane catalyst, *Appl. Catal. B-Environ.* 88 (2009) 550–556.
- [58] W. Guo, M. Zhang, Z. Lou, M. Zhou, P. Wang, H. Wei, Engineering nanoceria for enhanced peroxidase mimics: a solid solution strategy, *ChemCatChem* 11 (2018) 737–743.
- [59] G. Silversmit, D. Depla, H. Poelman, G.B. Marin, R.D. Gryse, Determination of the V2p XPS binding energies for different vanadium oxidation states (V⁵⁺ to V⁰⁺), *J. Electron. Spectrosc.* 135 (2004) 167–175.
- [60] S. Yang, W. Zhu, Z. Jiang, Z. Chen, J. Wang, The surface properties and the activities in catalytic wet air oxidation over CeO₂-TiO₂ catalysts, *Appl. Surf. Sci.* 252 (2006) 8499–8505.
- [61] L. Zhu, L. Zhang, H. Qu, Q. Zhong, A study on chemisorbed oxygen and reaction process of Fe-CuO_x/ZSM-5 via ultrasonic impregnation method for low-temperature NH₃-SCR, *J. Mol. Catal. A Chem.* 409 (2015) 207–215.
- [62] S. Zhang, H. Wang, H. Si, X. Jia, Z. Wang, Q. Li, J. Kong, J. Zhang, A. Novel, Core-shell (ϵ -MnO₂/CeO₂)/CeO₂ composite catalyst with synergistic effect for efficient formaldehyde oxidation, *ACS Appl. Mater. Interfaces* 12 (2020) 40285–40295.
- [63] H. Tan, W. Jin, S. Yu, K. Zhou, Support morphology-dependent catalytic activity of Pd/CeO₂ for formaldehyde oxidation, *Environ. Sci. Technol.* 49 (2015) 8675–8682.
- [64] C. Yang, X. Yang, T. Zhao, F. Liu, An indirect CO₂ utilization for the crystallization control of CaCO₃ using alkylcarbonate, *J. CO₂ Util.* 45 (2021), 101448.
- [65] X. Liu, X. Yang, H. Du, Y. Wu, X. Zhang, J. Zhang, Preparation and characterization of a porous silicate material using a CO₂-storage material for CO₂ adsorption, *Powder Technol.* 333 (2018) 138–152.
- [66] W. Yu, D. Hong, Y. Gao, X. Liu, T. Yang, L. Zhao, X. Yue, S. Zhang, J. Zhang, Syntheses of four novel silicate-based nanomaterials from coal gangue for the capture of CO₂, *Fuel* 258 (2019), 116192.
- [67] Y. Li, K.J. Zhang, Q. Du, F.F. Zhang, J.P. Gu, X.M. Liang, Cu/TiO₂ catalyzed wet oxidation of formaldehyde wastewater, *Technol. Water Treat.* 38 (2012) 101–104.
- [68] A.M.T. Silva, R.M. Quinta-Ferreira, J. Levec, Catalytic and noncatalytic wet oxidation of formaldehyde: a novel kinetic model, *Ind. Eng. Chem. Res.* 42 (2003) 5099–5108.
- [69] A.M.T. Silva, I.M.C. Branco, R.M.Q. Ferreira, J. Levec, Catalytic studies in wet oxidation of effluents from formaldehyde industry, *Chem. Eng. Sci.* 58 (2003) 963–970.
- [70] T. Zhao, G. Bo, Z. Fei, F. Sha, Q. Li, J. Zhang, Morphology control in the synthesis of CaCO₃ microspheres with a novel CO₂-storage material, *ACS Appl. Mater. Interfaces* 7 (2015) 15918–15927.
- [71] L. Zhao, J. Zhang, Intermolecular interaction of diamine-diol binary system: a mini-review, *Adv. Colloid Interfac.* 304 (2022), 102662.
- [72] L.Z. Pei, Y.Q. Pei, Y.K. Xie, C.G. Fan, H.Y. Yu, Synthesis and characterization of manganese vanadate nanorods as glassy carbon electrode modified materials for the determination of L-cysteine, *CrystEngComm* 15 (2013) 1729–1738.
- [73] N. Beermann, L. Vayssieres, S.E. Lindquist, A. Hagfeldt, Photoelectrochemical studies of oriented nanorod thin films of hematite, *J. Electrochem. Soc.* 147 (2000) 2456–2461.
- [74] T. Zhao, F. Zhang, J. Zhang, F. Sha, Q. Xu, B. Guo, X. Wei, Facile preparation of micro and nano-sized CaCO₃ particles by a new CO₂-storage material, *Powder Technol.* 301 (2016) 463–471.
- [75] Y. Liu, Y. Qian, Controllable synthesis of β -Mn₂V₂O₇ microtubes and hollow microspheres, *Mater. Lett.* 63 (2009) 28–30.
- [76] M.P. Andersson, F. Abild-Pedersen, I.N. Remedakis, T. Bligaard, G. Jones, J. Engbæk, O. Lytken, S. Hørch, J.H. Nielsen, J. Sehested, J.R. Rostrup-Nielsen, J. K. Nørskov, I. Chorkendorff, Structure sensitivity of the methanation reaction: H₂ induced CO dissociation on nickel surfaces, *J. Catal.* 255 (1) (2008) 6–19.
- [77] A. Selloni, Anatase shows its reactive side, *Nat. Mater.* 7 (8) (2008) 613–615.
- [78] C. Chen, E.C. Njagi, S.Y. Chen, D.T. Horvath, L. Xu, A. Morey, C. Mackin, R. Joesten, S.L. Suib, Structural distortion of molybdenum-doped manganese oxide octahedral molecular sieves for enhanced catalytic performance, *Inorg. Chem.* 54 (2015) 10163–10171.
- [79] T. Uematsu, Y. Miyamoto, Y. Ogasawara, K. Suzuki, K. Yamaguchi, N. Mizuno, Molybdenum-doped α -MnO₂ as an efficient reusable heterogeneous catalyst for aerobic sulfide oxygenation, *Catal. Sci. Technol.* 6 (2015) 222–233.
- [80] W. Gac, G. Slowik, W. Zawadzki, Structural and surface changes of copper modified manganese oxides, *Appl. Surf. Sci.* 370 (2016) 536–544.
- [81] M. Yu, W. Li, X. Li, X. Lin, T. Chen, J. Yan, Development of new transition metal oxide catalysts for the destruction of PCDD/Fs, *Chemosphere* 156 (2016) 383–391.
- [82] D.W. Kwon, K.B. Nam, S.C. Hong, Influence of tungsten on the activity of a Mn/Ce/W/Ti catalyst for the selective catalytic reduction of NO with NH₃ at low temperatures, *Appl. Catal. A Gen.* 497 (2015) 160–166.
- [83] P. Hu, Z. Amghouz, Z. Huang, F. Xu, Y. Chen, X. Tang, Surface-confined atomic silver centers catalyzing formaldehyde oxidation, *Environ. Sci. Technol.* 49 (2015) 2384–2390.
- [84] Y. Yang, J. Huang, S. Wang, S. Deng, B. Wang, G. Yu, Catalytic removal of gaseous unintentional POPs on manganese oxide octahedral molecular sieves, *Appl. Catal. B Environ.* 143 (2013) 567–568.
- [85] W. Si, Y. Wang, Z. Shen, F. Hu, J. Li, A facile method for *in situ* preparation of the MnO₂/LaMnO₃ catalyst for the removal of toluene, *Environ. Sci. Technol.* 50 (2016) 4572–4578.
- [86] X. Lin, S. Li, H. He, Z. Wu, J. Wu, L. Chen, D. Ye, M. Fu, Evolution of oxygen vacancies in MnO_x-CeO₂ mixed oxides for soot oxidation, *Appl. Catal. B-Environ.* 223 (2018) 91–102.
- [87] A. Lawrence, C.M. Jones, P. Wardman, M.J. Burkitt, Evidence for the role of a peroxidase compound I-type intermediate in the oxidation of glutathione, NADH, ascorbate, and dichlorofluorescein by cytochrome c/H₂O₂, *J. Biol. Chem.* 278 (2003) 29410–29419.
- [88] D. Chen, G. Zhang, M. Wang, N. Li, Q. Xu, H. Li, J. He, J. Lu, Pt/MnO₂ nanoflowers anchored to boron nitride aerogels for highly efficient enrichment and catalytic oxidation of formaldehyde at room temperature, *Angew. Chem. Int. Ed.* 60 (2021) 6377–6381.
- [89] J. Wang, P. Zhang, J. Li, C. Jiang, R. Yunus, J. Kim, Room-temperature oxidation of formaldehyde by layered manganese oxide: effect of water, *Environ. Sci. Technol.* 49 (2015) 12372.